Article

Fe-Doped Metal Complex (LaCo$_{0.9}$Fe$_{0.1}$O$_3$) and g-C$_3$N$_4$ Formed a Nanoheterojunction for the Photocatalytic Decomposition of Water

Kexin Zhang, Rui Wang, and Fubin Jiang*
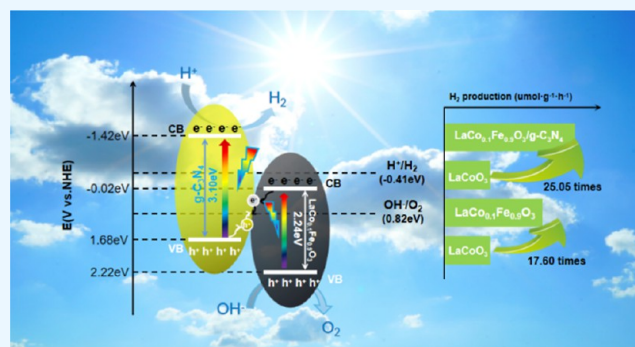
ACCESS | Metrics & More | Article Recommendations | SI Supporting Information

ABSTRACT: Photocatalytic water decomposition provides an environmentally friendly method of hydrogen production similar to "photosynthesis", while current research aims to develop affordable yet efficient photocatalysts. Oxygen vacancy is one of the most significant defects in metal oxide semiconductors, including perovskite, which substantially influences the semiconductor material's efficiency. To enhance the oxygen vacancy in the perovskite, we worked on doping Fe. A perovskite oxide nanostructure of LaCo$_x$Fe$_{1-x}$O$_3$ (x = 0.2, 0.4, 0.6, 0.8, and 0.9) was prepared by the sol−gel method, and a series of LaCo$_x$Fe$_{1-x}$O$_3$ (x = 0.2, 0.4, 0.6, 0.8, and 0.9)/g-C$_3$N$_4$ nanoheterojunction photocatalysts were synthesized using mechanical mixing and solvothermal methods for LaCo$_x$Fe$_{1-x}$O$_3$ (x = 0.2, 0.4, 0.6, 0.8, and

0.9). Fe was successfully doped into the perovskite (LaCoO$_3$), and the formation of an oxygen vacancy was verified by various detection methods. In our photocatalytic water decomposition experiments, we observed that LaCo$_{0.9}$Fe$_{0.1}$O$_3$ demonstrated a significant increase in its maximum hydrogen release rate, reaching 5249.21 μmol h^{-1} g^{-1}, which was remarkably 17.60 times higher than that of LaCoO$_3$-undoped Fe. Similarly, we also explored the photocatalytic activity of the nanoheterojunction complex LaCo$_{0.9}$Fe$_{0.1}$O$_3$/g-C$_3$N$_4$, and it exhibited pronounced performance with an average hydrogen production of 7472.67 μmol h^{-1} g^{-1}, which was 25.05 times that of LaCoO$_3$. We confirmed that the oxygen vacancy plays a crucial role in photocatalysis.

1. INTRODUCTION

Currently, the most pressing issue we encounter is increasing energy demand. Among various sustainable energy sources, hydrogen is one of the most promising energy sources.[1−3] Photocatalytic water splitting is a hydrogen production technology with high potential that makes use of photocatalysis to extract hydrogen from water, producing a clean fuel. To cope with the disadvantages of the high cost and scarcity of noble metal catalysts, the development of low-cost and efficient transition-metal oxide catalysts (such as perovskite materials) has become a research hotspot. Perovskite generally refers to oxides having the chemical formula ABO$_3$, which holds tremendous potential for applications such as sensors, magnetic reluctance devices, and catalysis.[4−9] At the same time, it is easy to form abundant oxygen vacancies, which is one of the most common defects in the list of semiconductor materials, especially in metal oxide semiconductors, and has an important effect on the performance of the list of semiconductor materials.[10] For example, LaCoO$_3$ perovskite has attracted wide attention due to its excellent properties and its invention applications including photocatalytic water splitting hydrogen production catalysts, sensors, electromagnetic wave absorption, solid oxide fuel cells, and so forth.[11−16] However, its wide band gap, small specific surface area, and fast electron−hole complexation are unfavorable for hydrogen

precipitation reactions. By modulating the metal cation or valence state at the B-site while increasing the number of oxygen defects, the catalytic activity of the catalyst can be modulated efficiently.[17,18] One of the most studied methods is to replace part of the B-site "Co" with iron. Tang and Wan[19,20] reported that Fe-doped nanostructures can be used for efficient electrochemical water splitting for hydrogen production with a hydrogen yield of 6.06 L min^{-1} g^{-1}. Dholam[21] tried to dope Fe and Cr into TiO$_2$, and the rate of photosplitting water to hydrogen gas was greatly improved, proving that the doping of Fe inhibits the direct recombination of electron−hole pairs. Hu et al.[22] observed that when Fe is doped, La$_2$Ti$_2$O$_7$ exhibits strong absorption in the visible light region, that is, the energy band structure changes.[23]

Recently, we have reported the performance of LaCoO$_3$/g-C$_3$N$_4$ in photocatalytic decomposition of water, and the rate of hydrogen generation under the full spectrum reaches 1046.15
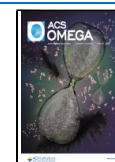
μmol h^{-1} g^{-1}.[24] Additionally, we investigated the photocatalytic ability of LaCoO$_3$/C$_3$N$_5$, and the hydrogen decomposition rate reached 956.11 μmol h^{-1} g^{-1}.[25] The two catalysts provide more choices for photocatalysis, but the decomposition rate of water may still be improved. We suggest that the oxygen vacancy may be responsible for the hindrance of water decomposition. It has been reported that the oxygen vacancy of the perovskite can effectively improve the recombination of electrons and holes and increase the photocatalytic performance.[26−29] Fe(III), as an effective solute cation, is often used in various catalytic reactions due to its special electronic structure of d-orbital half-filling.[30] With this in mind, we aim to dope LaCoO$_3$ with Fe and adjust the amount of the sacrificial agent according to the test. Through a large number of tests, we can prove that Fe is successfully doped and increases the oxygen vacancy. Our study found that the band gap of LaCo$_x$Fe$_{1−x}$O$_3$ after Fe doping is smaller, the specific surface area is reduced, and the ratio of M^{2+}/M^{3+} is increased by X-ray photoelectron spectroscopy (XPS) testing, with the introduction of oxygen defects.[18] This reduces the direct recombination of electron−hole pairs and effectively suppresses photogenerated electron−hole pair recombination.[9] However, even if we doped Fe, the problem of a small visible light range cannot be ignored; experiments show that C$_3$N$_4$ is an excellent visible light response catalyst,[31] We suspect that the perovskite and C$_3$N$_4$-formed heterojunction will be conducive to the response of visible light, so we have on this basis to carry out the synthesis of both. In this context, we synthesized LaCo$_x$Fe$_{1−x}$O$_3$ using a simple sol−gel method and then used mechanical stirring and dissolution heat to synthesize LaCo$_x$Fe$_{1−x}$O$_3$/g-C$_3$N$_4$ nanoheterojunction materials to study their properties of water to hydrogen production by photolysis in the presence of a full-spectrum irradiation reactor. The results show that the hydrogen release rate of LaCo$_{0.9}$Fe$_{0.1}$O$_3$ is the highest at 5249.21 μmol h^{-1} g^{-1}, which is 17.60 times that of undoped LaCoO$_3$. Meanwhile, the nanoheterojunction composite LaCo$_{0.9}$Fe$_{0.1}$O$_3$/g-C$_3$N$_4$ also showed excellent photocatalytic activity, and the average hydrogen production per hour was 7472.67 μmol h^{-1} g^{-1}, which was 25.05 times that of LaCoO$_3$. The existence of the oxygen vacancy proves to play an essential role in photocatalysis. The apparent quantum yield (AQY) is superior at 300−800 nm and was at most 3.85% under visible light.

2. EXPERIMENTAL SECTION

2.1. Materials. Lanthanum nitrate hexahydrate (AR), cobalt nitrate hexahydrate (AR), ferric nitrate hexahydrate (AR), citric acid (AR), urea (AR), anhydrous methanol (AR), and ethanol (AR) were obtained from Beijing Haoke Technology Co. , Ltd. All other reagents used in the synthesis were of analytical grade and used without further purification. Deionized water, with a resistivity of 18 MΩ cm, was used throughout the experiments.

2.2. Catalyst Preparation. *2.2.1. Preparation of LaCo$_x$Fe$_{1−x}$O$_3$ (x = 0.2, 0.4, 0.6, 0.8, and 0.9).*

(1) The mass of the reactant is calculated as the ratio of the amount of cobalt nitrate and ferric nitrate to the amount of lanthanum nitrate and citric acid, which is 1:1:2. The cobalt nitrate is 0.2910, 0.5821, 0.8731, 1.1641, and 1.3096 g; the contents of ferric nitrate were 0.1616, 1.2120, 0.8080, 0.4040, and 0.1010 g; lanthanum nitrate is 2.1651 g, and citric acid is 1.9210 g. Using 10 mL of

secondary water and 5 mL of ethanol to dissolve the substance, a deep red transparent solution was obtained. The preparation of the solution must avoid other ions mixing with the solution and the instrument before using secondary water several times.

(2) The deep red transparent solution was transferred to a round-bottom flask, heated in an 80 °C water bath, and stirred by magnetic force until the solution was in a deep red sol state.

(3) The deep red sol was poured into a clean ceramic crucible and dried at 120 °C for 6 h in a blast dryer to obtain a dark red expanded dry gel, which was fully ground for use.

(4) The ground powder was placed in a box muffle furnace and calcined from 5 °C min^{-1} to 400 °C for 4 h, then from 5 °C min^{-1} to 700 °C for 4 h, and at 700 °C for 4 h. After the machine cooled naturally, black LaCo$_x$Fe$_{1−x}$O$_3$ (x = 0.2, 0.4, 0.6, 0.8, and 0.9) powders were collected.

2.2.2. Preparation of g-C$_3$N$_4$. g-C$_3$N$_4$ was prepared by a simple thermal oxidation method of directly heating urea in a box muffle furnace. First, urea (5 g) was put into an open ceramic crucible, dried in a blast oven at 80 °C for 10 h, and ground to obtain dry urea powder. The ground urea powder was placed in a crucible with a LaCo$_x$Fe$_{1−x}$O$_3$ (x = 0.2, 0.4, 0.6, 0.8, and 0.9) lid, heated in a muffle furnace at a heating rate of 5 °C min^{-1} from 20 to 550 °C, and kept at this high temperature for 3 h. After cooling the product to 20 °C, a yellow powder was obtained and ground.

2.2.3. Preparation of LaCo$_x$Fe$_{1−x}$O$_3$ (x = 0.2, 0.4, 0.6, 0.8, and 0.9)/g-C$_3$N$_4$ Composites. Various weight ratios of LaCo$_x$Fe$_{1−x}$O$_3$ (x = 0.2, 0.4, 0.6, 0.8, and 0.9)/g-C$_3$N$_4$ were prepared by the solvothermal method (Figure S1). A certain weight of LaCo$_x$Fe$_{1−x}$O$_3$ (x = 0.2, 0.4, 0.6, 0.8, and 0.9) and of g-C$_3$N$_4$ were dispersed in anhydrous ethanol (10 mL) separately and sonicated for half an hour. The suspension of LaCo$_x$Fe$_{1−x}$O$_3$ (x = 0.2, 0.4, 0.6, 0.8, and 0.9) was slowly added to the suspension of g-C$_3$N$_4$. At room temperature, the mixed solution was sonicated for half an hour. During the process of ultrasonication, the system temperature was kept normal. The mixture was stirred at room temperature for 10 h and transferred to a clean hydrothermal kettle. The hydrothermal kettle was heated at 120 °C for 8 h. Finally, the mixture was centrifuged for half an hour and dried at 80 °C for 10 ho. LaCo$_x$Fe$_{1−x}$O$_3$ (x = 0.2, 0.4, 0.6, 0.8, and 0.9)/g-C$_3$N$_4$ nanoflakes with 20, 25, 30, 35, and 40 wt % LaCo$_x$Fe$_{1−x}$O$_3$ (x = 0.2, 0.4, 0.6, 0.8, and 0.9) contents were prepared by the above method.

2.3. Characterization. The surface morphology and microstructure were surveyed by scanning electron microscopy (SEM, HITACHI S-4800). With the help of a Shimadzu Maxima X-ray diffractometer (XRD 7000), the samples were irradiated by Cu Kα at a current of 30 mA and a voltage of 40 kV, and the crystal structure and phase composition of the samples were determined. The specific surface area, total pore volume, and average pore size of calcined perovskites were measured by N$_2$ physical adsorption at 77 K using a QUADRASORB Si (Quantachrome) adsorption analyzer. Before each surface area measurement, the 200 mg sample was degassed at 453 K for 3 h. The specific surface area of the material was calculated by the Brunauer−Emmett−Teller (BET) model, and the pore size distribution was calculated
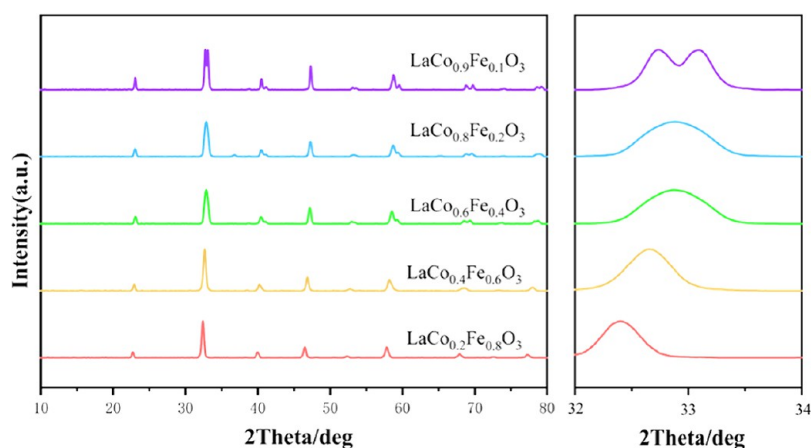
Figure 1. XRD patterns of $LaCo_xFe_{1-x}O_3$ (x = 0.20, 0.40, 0.60, 0.80, and 0.90).

from the desorption branch of the isotherm using the Barrett–Joyner–Halenda (BJH) method. Transmission electron microscopy (TEM, FEI Talos F200S) was used to characterize the spacing, and the growth of the material and the elemental distribution were characterized by energy-dispersive spectroscopy (EDS). XPS analysis was performed with a Thermo Fisher electron spectrometer (XPS, ESCALAB 250XI) equipped with a monochromatic microfocused Al Kα X-ray source, with the C 1s peak binding energy determined to be 284.8 eV for carbon correction. Fourier transform infrared (FT-IR) spectroscopy was measured by using an infrared spectrometer (Shimadzu IRAffinity-1). The optical properties of the samples were measured by UV−vis diffuse reflectance spectroscopy (DRS) using a UV-2600 spectrophotometer (Shimadzu, Japan) ($BaSO_4$ as the blank substrate). Photoluminescence (PL) spectral characterization was performed on an FS 980 photometer at room temperature using a 500 W xenon lamp source with an excitation wavelength of 300 nm. In a standard three-electrode system, a CHI1030C electrochemical workstation with a platinum mesh as the pair electrode, a silver/silver chloride electrode as the reference electrode, and 5 mg $LaCo_{0.9}Fe_{0.1}O_3$ were used. g-C_3N_4 and $LaCo_{0.9}Fe_{0.1}O_3$/g-C_3N_4-70 wt % were dissolved in a mixture of 800 μL distilled water, 200 μL isopropanol, and 30 μL Nafion. After ultrasonic treatment, it was dropped on a glassy carbon electrode employed as the working electrode. In addition, 0.1 mol/L $KHCO_3$ solution was used as the electrolyte. The width of the excitation and emission slits was 5 nm. The resistance of carrier migration was further investigated by electrochemical impedance spectroscopy (EIS) using 5 mmol L^{-1} Fe-$(CN)_6^{3-/4-}$ solution and 0.1 mol/L KCl solution as the electrolyte. The yield of H_2 was detected by manual injection on a Shimadzu gas chromatograph (GC-2014C). The electron paramagnetic resonance spectrum was measured by an electron paramagnetic resonance spectrometer (Bruker E500).

2.4. Full-Spectrum Photocatalytic Decomposition of Water for Hydrogen Production. The photocatalytic activity of the prepared samples was evaluated by photocatalytic hydrogen production from water decomposition. In this paper, all water decomposition experiments were carried out at a room temperature of 25 °C, and magnetic stirring was carried out during illumination. The light source was a 300 W xenon lamp (PLS-SXE300), and photocatalytic experiments were performed using full-spectrum (250 < λ < 1200 nm) simulated sunlight. The specific operation was as follows: first,

10 mg of catalyst was placed into a custom-made quartz round-bottom flask, and 80 mL of water was added for ultrasonic treatment, making it evenly dispersed in the water solution. Then, 20 mL of anhydrous methanol was added as a sacrificial agent. After adding magnetons, nitrogen was introduced for 60 min to remove dissolved oxygen from the solution in the condition of protecting from light. A full-spectrum xenon lamp was used to illuminate the container filled with nitrogen gas with a rubber plug. The irradiation duration of the xenon lamp was set to 5 h, and the irradiation current was set to 18.5 A. Then, the "RUN" button was pressed to operate the xenon lamp, cycling five times.

It is worth mentioning that the process of photocatalysis always uses magnetic stirring so that the catalyst in the solution is evenly dispersed to prevent catalyst deposition at the bottom of the vessel, which can affect the catalytic effect. Due to the use of a full-spectrum irradiation reactor, light energy is higher. It is easy for this to result in a shorter-time temperature rise too quickly, which can increase the number of variables that affect the response. Therefore, we use the cooling circulating water system to maintain a relatively stable reaction temperature in the photocatalytic process. Generally, the temperature of the cooling circulating water is set to 20 °C, and the cooling circulating water cools the vessel through the outside of the reaction vessel so that the inside of the vessel maintains a reaction environment close to room temperature. The H_2 production rate was monitored hourly by a gas chromatograph equipped with a molecular sieve column and a TCD detector. Each material underwent three photocatalytic experiments to eliminate unexpected factors and enhance the reliability of the experimental data. The optimum ratio of the photocatalyst was determined, and the stability of the photocatalyst was tested. The photocatalyst was tested five times in a cycle of 5 h for a total of 25 h. Apparent quantum efficiency was computed using the following equation

$$\text{AQY (\%)} = \frac{2 \times \text{number of evolved hydrogen molecules}}{\text{number of incident photons}}$$
$$\times 100\% \quad\quad (1)$$

3. RESULTS AND DISCUSSION

3.1. X-ray Diffraction Analysis. The crystal structure of $LaCo_xFe_{1-x}O_3$ (x = 0.2, 0.4, 0.6, 0.8, and 0.9) powder was characterized by X-ray diffraction (XRD), as shown in Figure

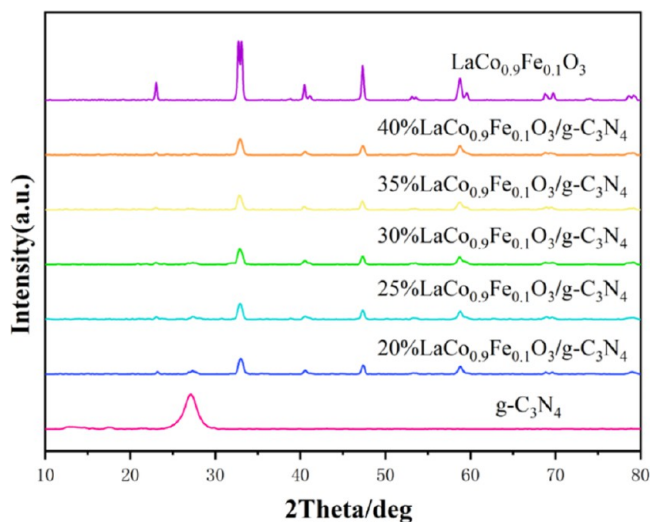**Figure 2.** XRD patterns of g-C_3N_4, $LaCo_{0.9}Fe_{0.1}O_3$ and 20, 25, 30, 35, and 40 wt %-$LaCo_{0.9}Fe_{0.1}O_3$/g-C_3N_4.
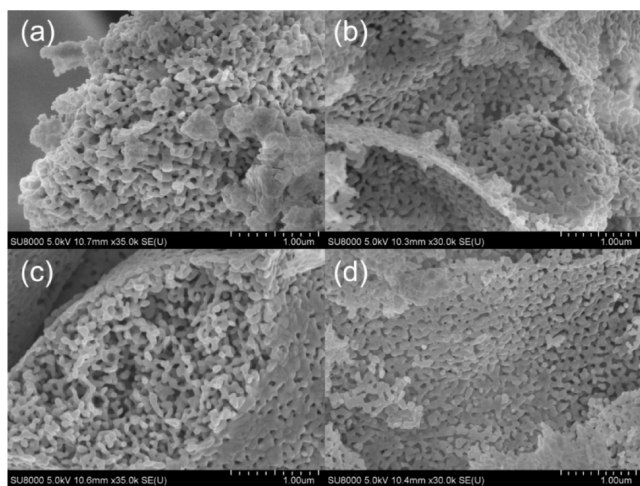
Figure 3. (a) $LaCo_{0.2}Fe_{0.8}O_3$, (b) $LaCo_{0.4}Fe_{0.6}O_3$, (c) $LaCo_{0.6}Fe_{0.4}O_3$, and (d) $LaCo_{0.8}Fe_{0.2}O_3$ SEM images.
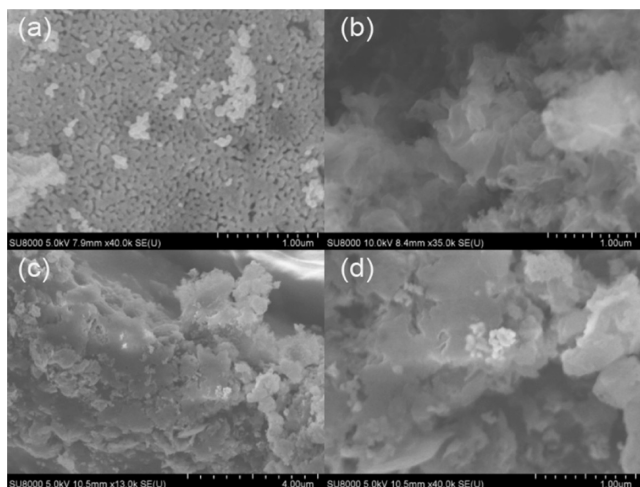
Figure 4. (a) $LaCo_{0.9}Fe_{0.1}O_3$, (b) g-C_3N_4, and (c,d) $LaCo_{0.9}Fe_{0.1}O_3$/g-C_3N_4-70 wt % SEM images.
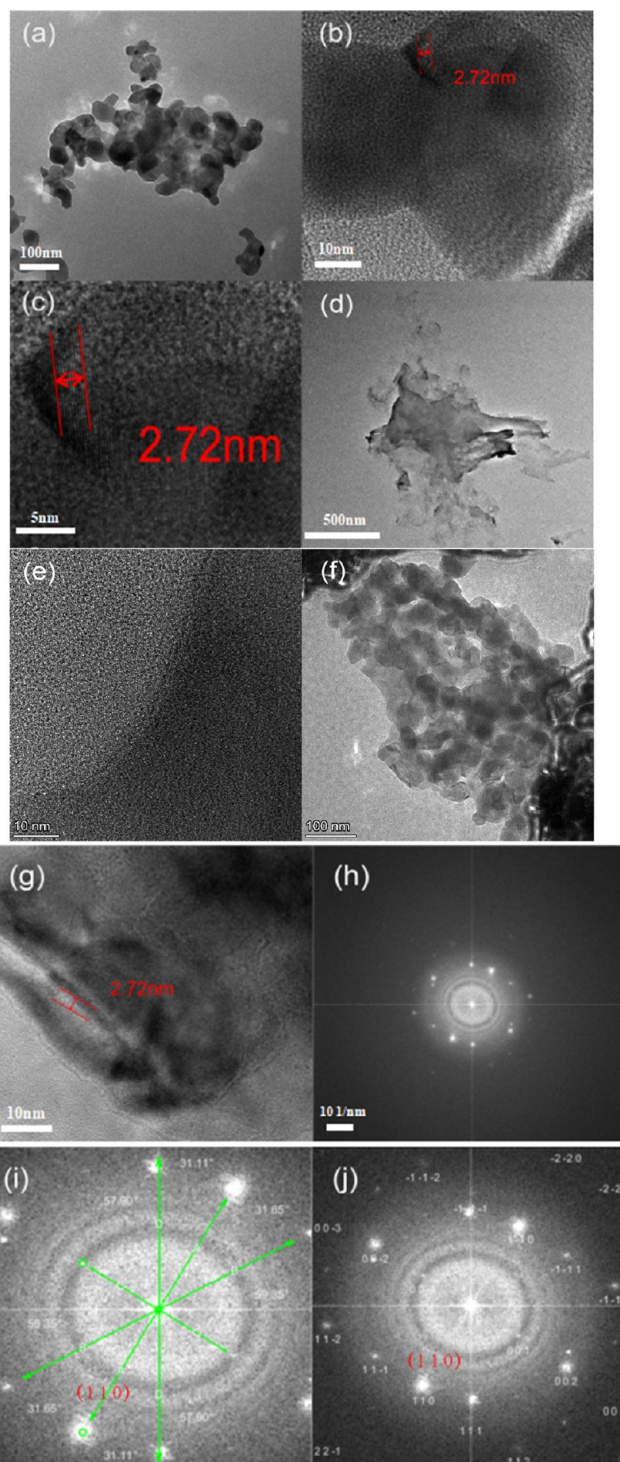
Figure 5. (a) TEM image and (b,c) HRTEM image of $LaCo_{0.9}Fe_{0.1}O_3$; (d) TEM image and (e) HRTEM images of g-C_3N_4; (f) TEM image, (g) HRTEM image, and (h–j) SAED mode images of $LaCo_{0.9}Fe_{0.1}O_3$/g-C_3N_4-70 wt %.

1. The distinct peaks of $LaCo_xFe_{1-x}O_3$ are in line with the characteristic peak of JCPDS no. 44-0361, JCPDS no. 53-1211, JCPDS no. 40-0224. Upon analysis of the characteristic peaks, it can be observed that there are no discernible impurities present in the results. Additionally, the level of crystallinity exhibited in the analysis is of high quality.[32−34] As Fe-to-Co partial substitution increases, the intensity of the characteristic peaks increases, and the splitting peaks merge into a single

Figure 6. SEM image of the selected area of $LaCo_{0.9}Fe_{0.1}O_3$ and the corresponding EDX mapping images for La, Co, Fe, and O elements.

peak and move toward lower angles. This is because the covalent radius of Fe^{3+} (LS 132 pm, HS 152 pm) is larger than that of Co^{3+} (LS 126 pm, HS 150 pm).[35] In addition, when the doping ratio of Fe is 0.8 and 0.6, the perovskite is orthorhombic. When the doping ratio is 0.4 and 0.2, the perovskite is 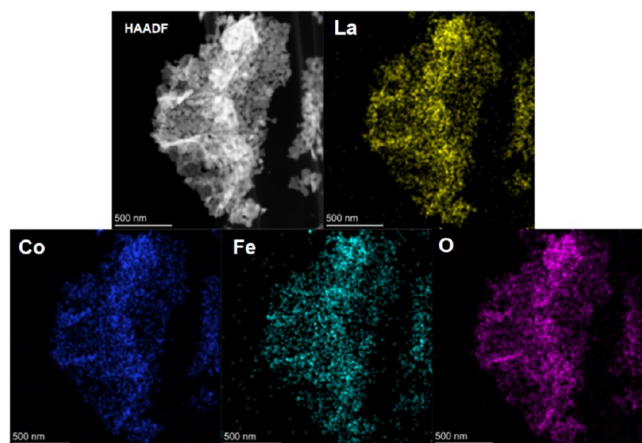a mixed structure of orthorhombic and triangular shapes, respectively. When the ratio is 0.1, its structure is a triangular system, which indicates that the doping of Fe changes the lattice structure.[32,33]

The crystal structures of g-C_3N_4, $LaCo_{0.9}Fe_{0.1}O_3$, and $LaCo_{0.9}Fe_{0.1}O_3$/g-C_3N_4 with various weight ratios were

characterized by XRD, as shown in Figure 2. The XRD of g-C_3N_4 displays two main peaks at 13.1 and 27.7°.[36] The stronger peak is at 27.7° from the (0 0 2) crystal plane of layered g-C_3N_4, while the weaker peak is at 13.1° from the in-plane (1 0 0) crystal plane (JCPDS no. 87-1526). The XRD peak of $LaCo_{0.9}Fe_{0.1}O_3$ is highly consistent with the crystal phase of JCPDS no. 44-0361, and the characteristic peak at 32.8° is attributed to the (1 1 0) crystal plane.[32] Behind the combination of $LaCo_{0.9}Fe_{0.1}O_3$ and g-C_3N_4, the characteristic peak intensities of $LaCo_{0.9}Fe_{0.1}O_3$ and g-C_3N_4 are significantly reduced, which once again proves that the nanoheterojunction composite was successfully prepared.

3.2. SEM Analysis. It can be seen from Figure 3a−d that $LaCo_xFe_{1−x}O_3$ (x = 0.2, 0.4, 0.6, 0.8, and 0.9) obtained by the sol−gel method is composed of many ellipsoids, among which the ellipsoid particles are $LaCo_{0.9}Fe_{0.1}O_3$. The particle size is the most uniform, and the particles grow most closely together to form a two-dimensional nanolayered structure, as shown in Figure 4a.[37] In Figure 4b, the synthesis of the g-C_3N_4 utilized urea as the precursor material through a process of calcination. The resulting structure of the g-C_3N_4 takes the form of a lamellar tremella, with each individual lamella possessing a flat surface ideal for use as a substrate material. From Figure 4c,d, we can observe that the $LaCo_{0.9}Fe_{0.1}O_3$ nanoparticle layer is dispersed as particles and grows in clusters on g-C_3N_4. This staggered structure has a larger surface area, which is conducive to the absorption and utilization of light energy by the catalyst. Both the surface and the interior can receive light sources, which increases the number of active sites for photosplitting water to produce hydrogen.
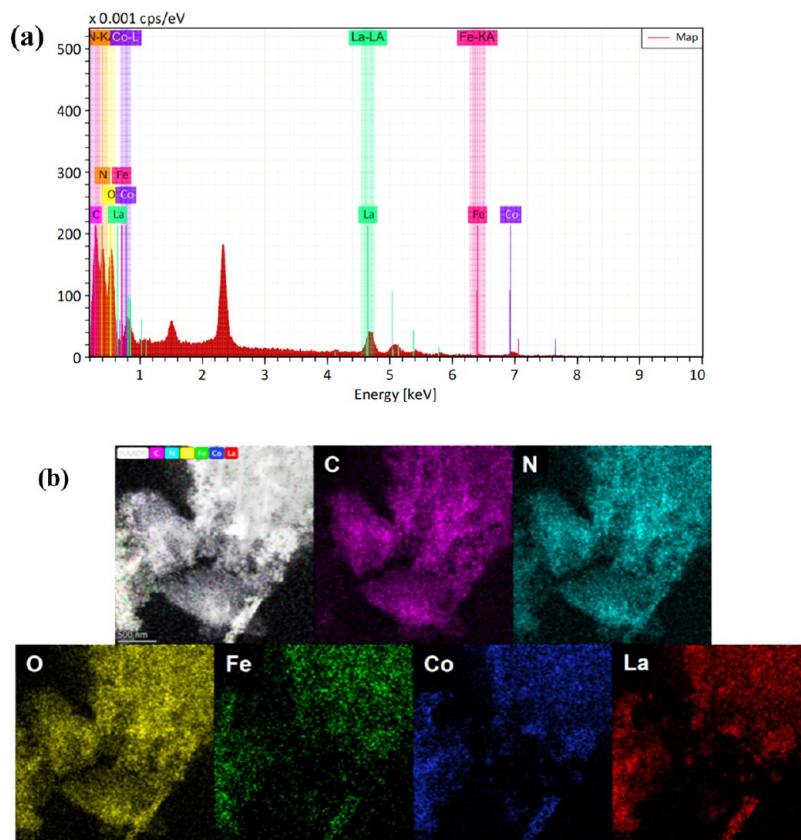

Figure 7. (a) EDX spectra of $LaCo_{0.9}Fe_{0.1}O_3$/g-C_3N_4-70 wt %, (b) SEM image of the selected area of $LaCo_{0.9}Fe_{0.1}O_3$/g-C_3N_4-70 wt %, and the corresponding EDX mapping images for C, N, O, Fe, Co, and La elements.
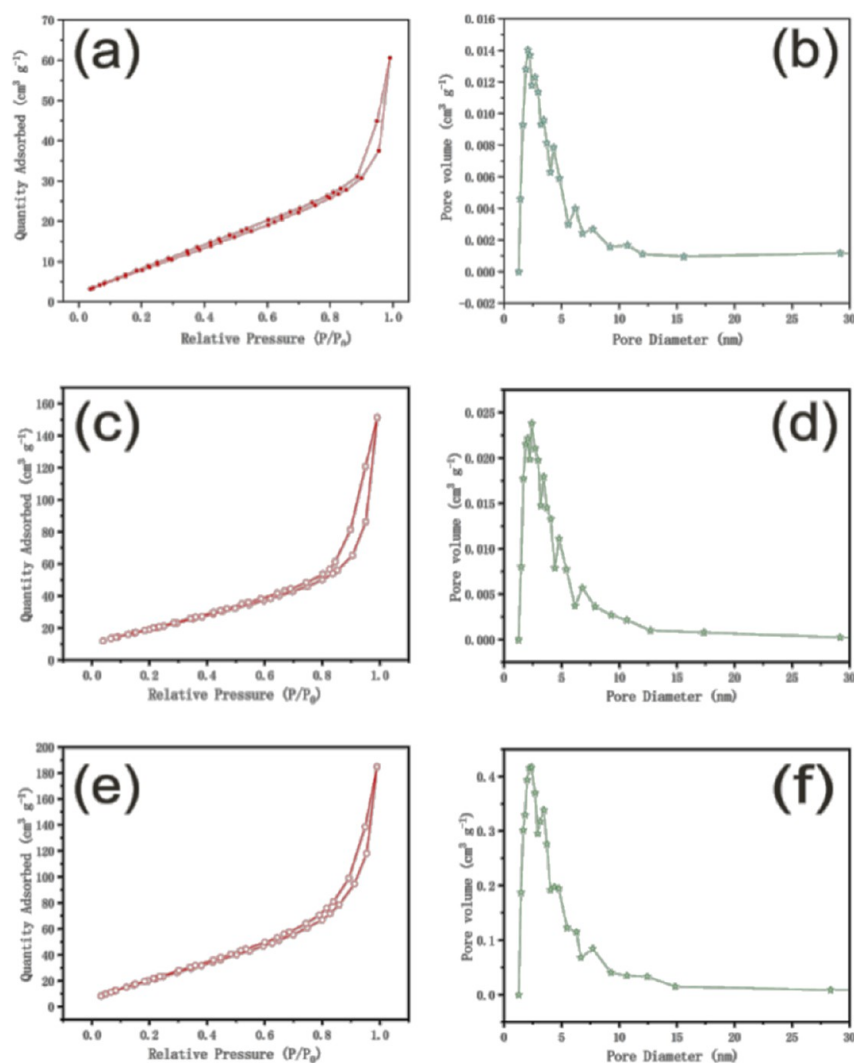
Figure 8. N_2 adsorption/desorption isotherms and pore size distribution curves (a,b) BET surface area analysis and BJH pore size analysis images of $LaCo_{0.9}Fe_{0.1}O_3$; (c,d) BET surface area analysis and BJH pore size analysis images of g-C_3N_4; (e,f) BET surface area analysis and BJH pore size analysis of $LaCo_{0.9}Fe_{0.1}O_3/g$-C_3N_4-70 wt %.

Table 1. Parameters of the Surface Physical Structure of $LaCo_{0.9}Fe_{0.1}O_3$, g-C_3N_4 and $LaCo_{0.9}Fe_{0.1}O_3/g$-C_3N_4-70 wt %

catalyst	BET surface area (m^2 g^{-1})	total pore volume (cm^3 g^{-1})	diameters of the pore (nm)
$LaCo_{0.9}Fe_{0.1}O_3$	64.99	0.11	2.07
g-C_3N_4	100.69	0.10	2.41
$LaCo_{0.9}Fe_{0.1}O_3/g$-C_3N_4-70 wt %	153.87	0.315	2.19

3.3. TEM Analysis. After that, we verified the morphology, elemental composition, composition structure, particle size, and other characteristics of the catalyst by TEM and high-resolution TEM (HRTEM) to explore the influence on its properties. The $LaCo_{0.9}Fe_{0.1}O_3$ in Figure 5a shows an obvious ellipsoid structure with an ellipsoid particle size distribution ranging from 60 to 80 nm. In Figure 5b,c, we can observe that the well-crystallized $LaCo_{0.9}Fe_{0.1}O_3$ nanoparticles have obvious lattice spacing (d value), and the spacing between adjacent lattice fringes is fixed. The distance between adjacent lattice fringes, that is, the plane spacing, is about 0.272 nm, which is consistent with the crystal plane (1 1 0). As shown in Figure

5d,e, g-C_3N_4 exhibited a distinct layered structure, consistent with the above observations. In Figure 5f,g, lattice plane separation can be observed at the interface, and the plane spacing between adjacent lattice fringes is approximately 0.27 nm, which is consistent with (1 1 0). The crystal plane index (1 1 0) of $LaCo_{0.9}Fe_{0.1}O_3$ obtained by XRD analysis is consistent with the obvious diffraction peaks in the SAED mode, as shown in Figure 5h−j. Figure 6 shows EDS, which verifies the composition of elements in $LaCo_{0.9}Fe_{0.1}O_3$, and no other elements are found. The elemental composition and distribution of $LaCo_{0.9}Fe_{0.1}O_3/g$-C_3N_4-70 wt % are shown in Figure 7, and La, Co, Fe, C, N, and O are all uniformly distributed.

3.4. BET Surface Area and BJH Pore Size Distribution Analysis. According to the SEM image and TEM image of $LaCo_{0.9}Fe_{0.1}O_3$, we can see that it is in the form of spherical particles. The specific area, average pore size, and average particle size of the samples were measured by the BET technique. Figure 8a,c,e shows that the nitrogen adsorption analytical isotherms of g-C_3N_4, $LaCo_{0.9}Fe_{0.1}O_3$, and La-$Co_{0.9}Fe_{0.1}O_3/g$-C_3N_4 are inconsistent with the desorption curves, and there is a hysteresis ring. In line with the
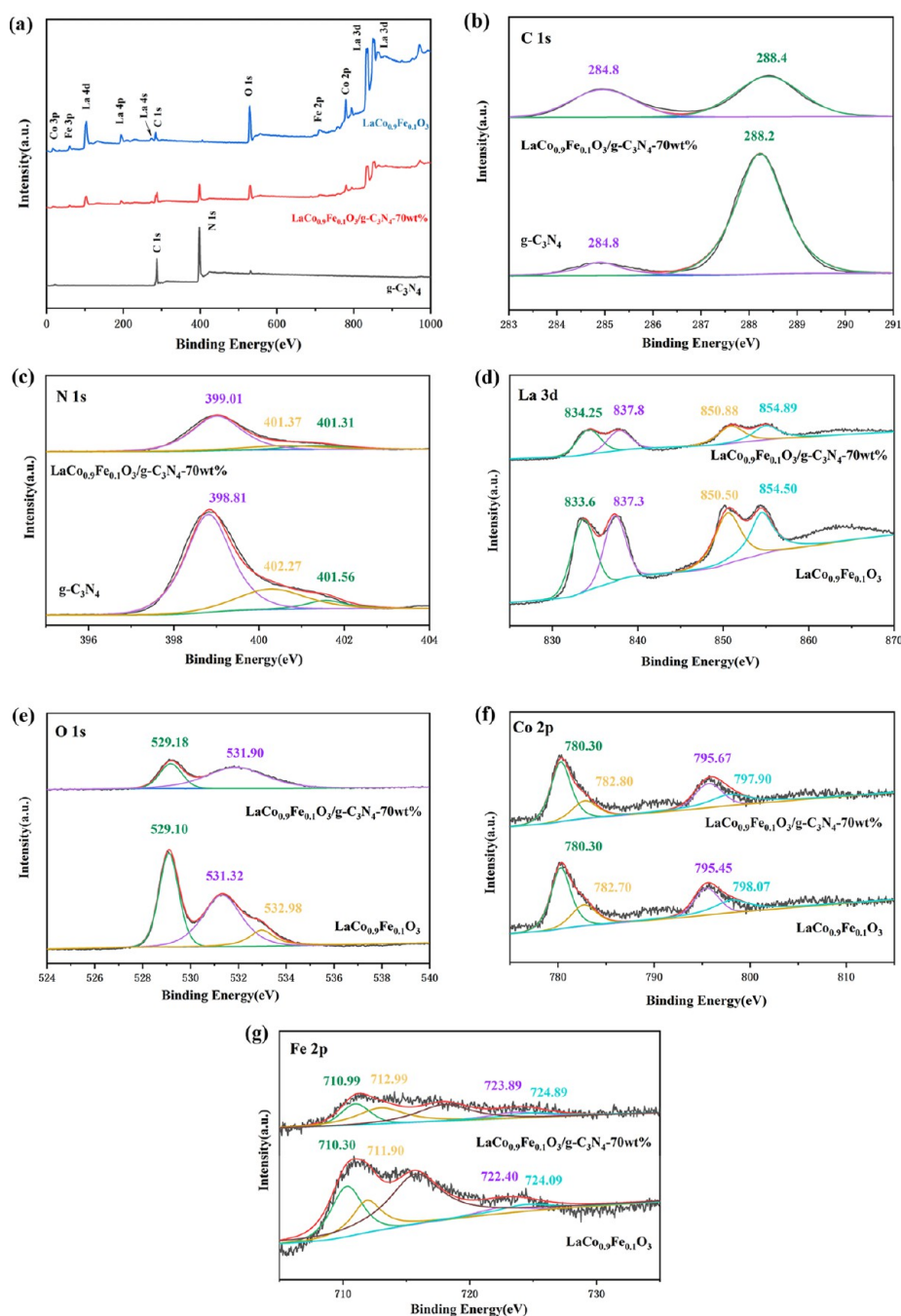
Figure 9. (a) XPS full spectrum of pure $LaCo_{0.9}Fe_{0.1}O_3$, pure g-C_3N_4, and $LaCo_{0.9}Fe_{0.1}O_3$/g-C_3N_4-70 wt %; high-resolution spectra of (b) C 1s and (c) N 1s of pure g-C_3N_4 and $LaCo_{0.9}Fe_{0.1}O_3$/g-C_3N_4-70 wt %; high-resolution spectra of (d) La 3d, (e) O 1s, (f) Co 2p, and (g) Fe 2p of pure $LaCo_{0.9}Fe_{0.1}O_3$ and $LaCo_{0.9}Fe_{0.1}O_3$/g-C_3N_4-70 wt %.

Table 2. XPS Binding Energies of $LaCo_{0.9}Fe_{0.1}O_3$, g-C_3N_4, and $LaCo_{0.9}Fe_{0.1}O_3$/g-C_3N_4-70 wt %

	Co 2p		Fe 2p		O 1s	
	Co 2p$_{3/2}$	Co 2p$_{1/2}$	Fe 2p$_{3/2}$	Fe 2p$_{1/2}$		
$LaCoO_3$	779.8 (67%) Co^{2+}	794.9 (33%) Co^{2+}	Fe^{2+} Fe^{3+}	Fe^{2+} Fe^{3+}	528.7 (45%)	530.9 (40%)
$LaCo_{0.9}Fe_{0.1}O_3$	780.3 (53%) 782.7 (47%)	795.4 (64%) 794.9 (36%)	710.3 711.9	722.4 724.3	529.1 (43%)	531.3 (44%)
$LaCo_{0.9}Fe_{0.1}O_3$/g-C_3N_4-70 wt %	780.3 (55%) 782.8 (44%)	795.6 (69%) 797.9 (31%)	710.9 712.9	723.5 724.9	529.2 (40%)	531.9 (59%)

characteristics of the type IV adsorption equilibrium isotherm, all are mesoporous materials.[38] Table 1 shows that the pore size of the sample is concentrated in the range of 2−3 nm, which belongs to mesopores, which is also consistent with the

Figure 10. Left: FT-IR spectra of $LaCo_xFe_{1-x}O_3$ (x = 0.20, 0.40, 0.60, 0.80, and 0.90). Right: FT-IR spectra of g-C_3N_4, $LaCo_{0.9}Fe_{0.1}O_3$, and 25, 30, 35, 40 wt %-$LaCo_{0.9}Fe_{0.1}O_3$/g-C_3N_4.
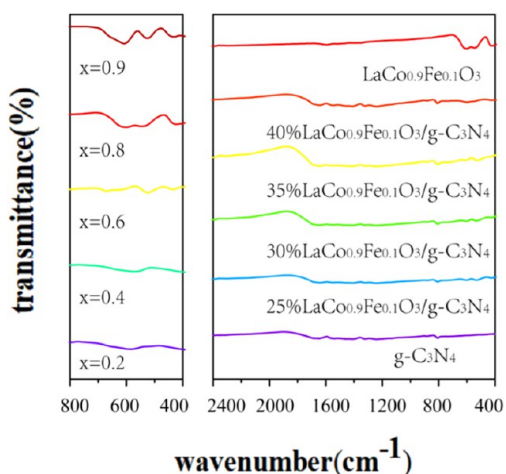
above adsorption and desorption isotherm analysis results. The specific surface areas of $LaCo_{0.9}Fe_{0.1}O_3$, g-C_3N_4 and $LaCo_{0.9}Fe_{0.1}O_3$/g-C_3N_4-70 wt % are 64.99, 100.69, and 153.87 m^2 g^{-1}, respectively. The specific surface area of $LaCo_{0.9}Fe_{0.1}O_3$/g-C_3N_4-70 wt % is 2.4 times that of $LaCo_{0.9}Fe_{0.1}O_3$ and 1.5 times that of g-C_3N_4. That is, the combination of the two is beneficial for increasing the number of active sites, so as to improve the photocatalytic water splitting activity.

3.5. XPS Analysis. We analyzed the XPS spectrum for obtaining the chemical state and the interaction, as shown in Figure 9a, with carbon correction for the C 1s peak at 284.8 eV. The $LaCo_{0.9}Fe_{0.1}O_3$/g-C_3N_4-70 wt % composite is composed of La, Co, Fe, O, C, and N. The high-resolution C 1s spectrum of pure g-C_3N_4 can be separated into two major peaks located at nearly 284.8 and 288.2 eV. The C 1s peak at 284.8 eV is attributed to the C−C bond of carbon, and the peak at 288.2 eV is attributed to the sp^2-type C=N bond.[39,40] The high-resolution N 1s spectrum of the g-C_3N_4 sample shown in Figure 9c can be divided into three major peaks. We assigned the N 1s peak corresponding to the lowest binding energy (398.8 eV) for the C−N bond and a central peak of 400.2 eV for the sp^2-type C=N bond.[41] The peak with the largest binding energy is at 401.5 eV, which arises from nitrogen surrounded by three carbons in the amorphous CN network.

Note that the characteristic peak of the N−(C)$_3$ bond in the $LaCo_{0.9}Fe_{0.1}O_3$/g-C_3N_4-70 wt % spectrum is redshifted by 0.2 eV. This indicates that the electron density increases after $LaCo_{0.9}Fe_{0.1}O_3$ is combined with g-C_3N_4. The high-resolution O 1s XPS spectrum has two main features at approximately 529.1 and 531.9 eV. The spectrum of the pure $LaCo_{0.9}Fe_{0.1}O_3$ sample can be divided into three peaks: the peak with the lowest binding energy (approximately 529.1 eV) is due to the lattice oxygen atoms on the surface; the next peak (approximately 531.3 eV) is attributed to surface-adsorbed oxygen, and the peak with the highest binding energy (approximately 532.9 eV) is attributed to adsorbed water. The high-resolution O 1s spectrum of $LaCo_{0.9}Fe_{0.1}O_3$/g-C_3N_4 exhibits two main features at 529.1 and 531.9 eV, which are attributed to the surface lattice oxygen atoms and the surface adsorbed oxygen, respectively.[42] Among them, the peak

position of surface-adsorbed oxygen bonds in the spectrum of $LaCo_{0.9}Fe_{0.1}O_3$/g-C_3N_4-70 wt % increased by 0.6 eV, and the occupied area increased, which indicated that after combining with $LaCo_{0.9}Fe_{0.1}O_3$, the adsorbed oxygen content in $LaCo_{0.9}Fe_{0.1}O_3$/g-C_3N_4 increased significantly. The typical high-resolution XPS La 3d spectrum of the $LaCo_{0.9}Fe_{0.1}O_3$/g-C_3N_4-70 wt % sample shows two shoulder peaks with vibrational features at 830−840 and 850−857 eV, which can be split into two distinct peaks located at 834.2 and 837.8 and 850.8 and 854.8 eV, corresponding to the binding energies of La 3d$_{5/2}$ and La 3d$_{3/2}$, respectively, confirming the existence of La^{3+} in the crystal structure.[43−45] For the high-resolution Co 2p spectrum of the $LaCo_{0.9}Fe_{0.1}O_3$/g-C_3N_4-70 wt % sample (Figure 9f), there are two main peaks located at 780.3 and 795.6 eV, which are attributed to the typical Co^{3+} structure at 787.2 eV typical of shaking.[46] In addition, there are two satellite peaks at 782.8 and 797.9 eV. There are two shoulder peaks in the high-resolution Fe 2p spectrum (Figure 9g), which are at 710.9 and 712.9, 723.8, and 724.8 eV, corresponding to the binding energies of Fe 2p$_{3/2}$ and Fe 2p$_{5/2}$, respectively. There is also a satellite peak at 717.9 eV.[47] From Table 2, we can see that with Fe doping, the ratio of M^{2+}/M^{3+} increases, enriching oxygen vacancies (OVs) and suppressing direct electron−hole recombination.[18] In short, the XPS results further demonstrate that $LaCo_{0.9}Fe_{0.1}O_3$/g-C_3N_4 composites were successfully obtained and that the main electron transfer pathway was from $LaCo_{0.9}Fe_{0.1}O_3$ to g-C_3N_4.

3.6. FT-IR Absorption Analysis. The FT-IR spectrum of $LaCo_xFe_{1-x}O_3$ (x = 0.2, 0.4, 0.6, 0.8, and 0.9) is shown on the left side of Figure 10. The absorption band at 600 cm^{-1} is attributed to the Co−O stretching vibration, and there is a strong vibrational band at 574 cm^{-1}, which may be derived from the characteristic absorption bands of the Fe−O stretching vibration and the O−Fe−O bending vibration.[48,49] The FT-IR spectra of $LaCo_{0.9}Fe_{0.1}O_3$, g-C_3N_4, and 25, 30, 35, and 40 wt % $LaCo_{0.9}Fe_{0.1}O_3$/g-C_3N_4 are shown on the right side of Figure 10. For pure g-C_3N_4, the characteristic peaks at 1508.4, 1541.2, and 1558.6 cm^{-1} are consistent with aromatic-CN stretching vibrational modes. In addition, the breathing vibration of g-C_3N_4 appears as a characteristic absorption peak at 810 cm^{-1}, corresponding to the breathing vibration peak in g-C_3N_4 (tri-triazine unit) and the deformation vibration peak of surface N−H.[50] The characteristic peaks of $LaCo_{0.9}Fe_{0.1}O_3$ at 600 and 560 cm^{-1} are related to the bending and stretching vibrations of Co−O, corresponding to the perovskite structure.[48] As the content of g-C_3N_4 in the $LaCo_{0.9}Fe_{0.1}O_3$ sample increases, the characteristic peaks of the composites gradually become sharper. Furthermore, the spectrum of the $LaCo_{0.9}Fe_{0.1}O_3$/g-C_3N_4 sample shows a blueshift at 810 cm^{-1} (tris-triazine unit) compared to the spectrum of g-C_3N_4. This indicates that the number of hydrogen bonds in the g-C_3N_4 structure is reduced, which will facilitate the transfer of charge carriers in the carbon nitride layer.

3.7. UV−vis DRS and Mott−Schottky Plot Analysis. As shown in Figure 11b, the solid UV diffuse reflectances of pure $LaCo_{0.9}Fe_{0.1}O_3$, g-C_3N_4, and $LaCo_{0.9}Fe_{0.1}O_3$/g-C_3N_4-70 wt % were measured by solid UV diffuse reflectance spectroscopy in the range of 220−800 nm. Obviously, g-C_3N_4 has the strongest absorption for ultraviolet light, and its visible spectral absorption edge is approximately 470 nm, which is consistent with the known reports. The $LaCo_{0.9}Fe_{0.1}O_3$/g-C_3N_4 composite has similar absorption properties to g-C_3N_4. Almost all ranges of light can be absorbed by pure $LaCo_{0.9}Fe_{0.1}O_3$, which
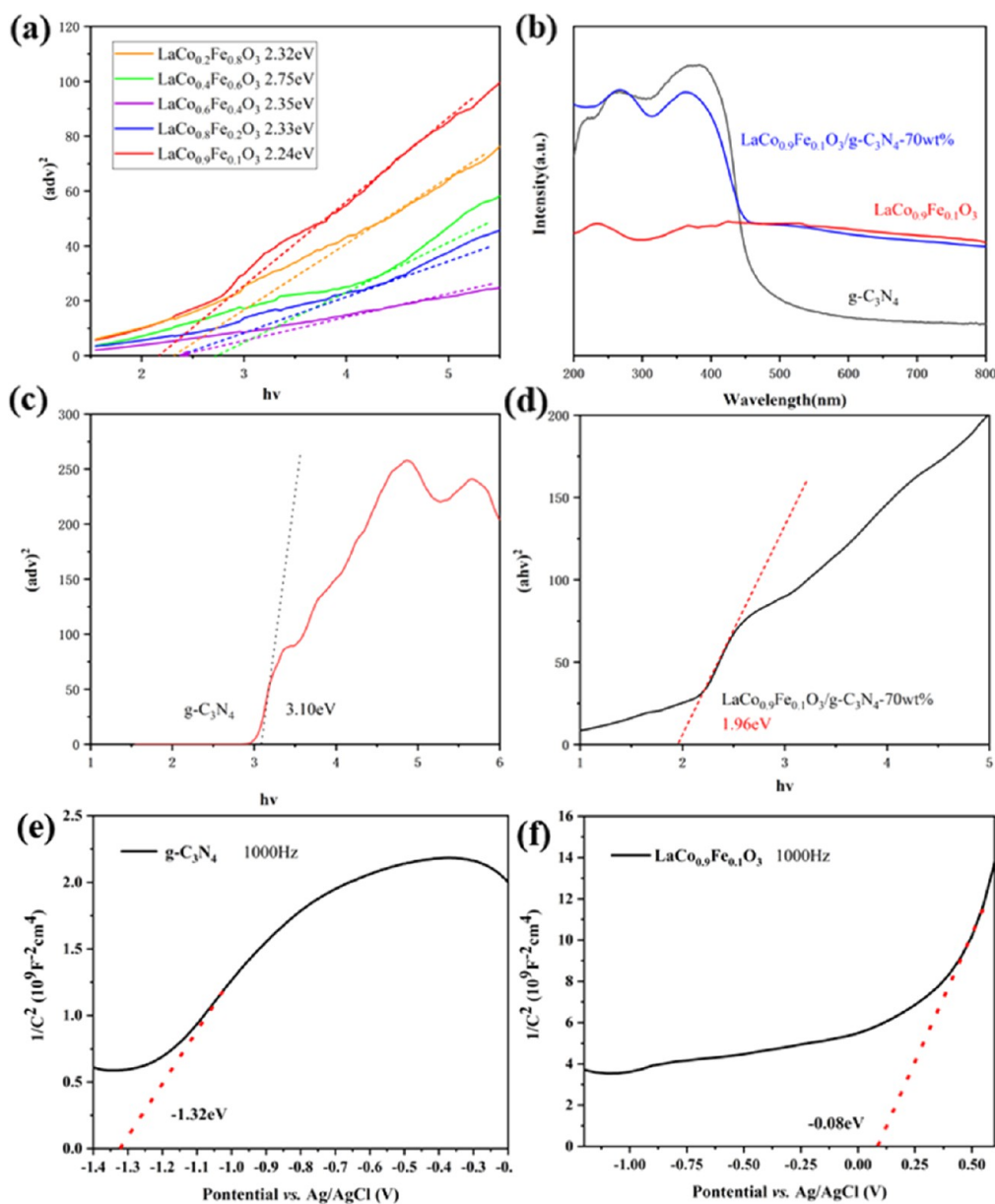
Figure 11. (a) Plots of band gap energies (E_gs) for LaCo$_x$Fe$_{1-x}$O$_3$; (b) UV−vis DRS spectra of LaCo$_{0.9}$Fe$_{0.1}$O$_3$, g-C$_3$N$_4$, and LaCo$_{0.9}$Fe$_{0.1}$O$_3$/g-C$_3$N$_4$-70 wt % composites; (c) plots of band gap energies (E_gs) for g-C$_3$N$_4$; (d) plots of gap energies (E_gs) for LaCo$_{0.9}$Fe$_{0.1}$O$_3$/g-C$_3$N$_4$-70 wt %; (e,f) M−S plots collected under 1000 Hz of g-C$_3$N$_4$ and LaCo$_{0.9}$Fe$_{0.1}$O$_3$.

Table 3. LaCo$_{0.9}$Fe$_{0.1}$O$_3$ and g-C$_3$N$_4$ Band Gaps

sample	χ (eV)	E_{CB} (eV)	E_{VB} (eV)	E_g
LaCo$_{0.9}$Fe$_{0.1}$O$_3$	5.60	−0.02	2.22	2.24
g-C$_3$N$_4$	4.63	−1.42	1.68	3.10

shows the excellent optoelectronic properties of La-Co$_{0.9}$Fe$_{0.1}$O$_3$. Note that the absorption edge of the LaCo$_{0.9}$Fe$_{0.1}$O$_3$/g-C$_3$N$_4$ composite is redshifted compared with that of pure g-C$_3$N$_4$, which indicates that the LaCo$_{0.9}$Fe$_{0.1}$O$_3$/g-C$_3$N$_4$ composite can absorb more visible light.

The band gap energy (E_g) of a semiconductor is determined according to the Kubelka−Munk equation as follows

$$(\alpha h\nu)^{1/n} = A(h\nu - E_g) \tag{2}$$

Here, α, h, ν, A, E_g, and n represent the absorption coefficient, Planck constant, incident light frequency, constant, band gap, and integer, respectively. Figure 11a shows the band gap energy (E_g) of LaCo$_x$Fe$_{1-x}$O$_3$ (x = 0.20, 0.40, 0.60, 0.80, and 0.90); Figure 11a,c,d shows the calculated band gap E_g values of g-C$_3$N$_4$, LaCo$_{0.9}$Fe$_{0.1}$O$_3$, and LaCo$_{0.9}$Fe$_{0.1}$O$_3$/g-C$_3$N$_4$, which are approximately 3.10, 2.24, and 1.96 eV, respectively. The E_g values obtained from the composites are smaller. Alternatively, the VB and CB potentials of semiconductors can also be obtained from the following empirical formulas

$$E_{CB} = \chi - E^\theta - 0.5E_g \tag{3}$$

$$E_{VB} = E_{CB} + E_g \tag{4}$$

E_{CB} and E_{VB} represent the CB and VB edge potentials of the semiconductor, respectively. χ is the electronegativity of a semiconductor.[51] According to ref 47, the χ values of pure
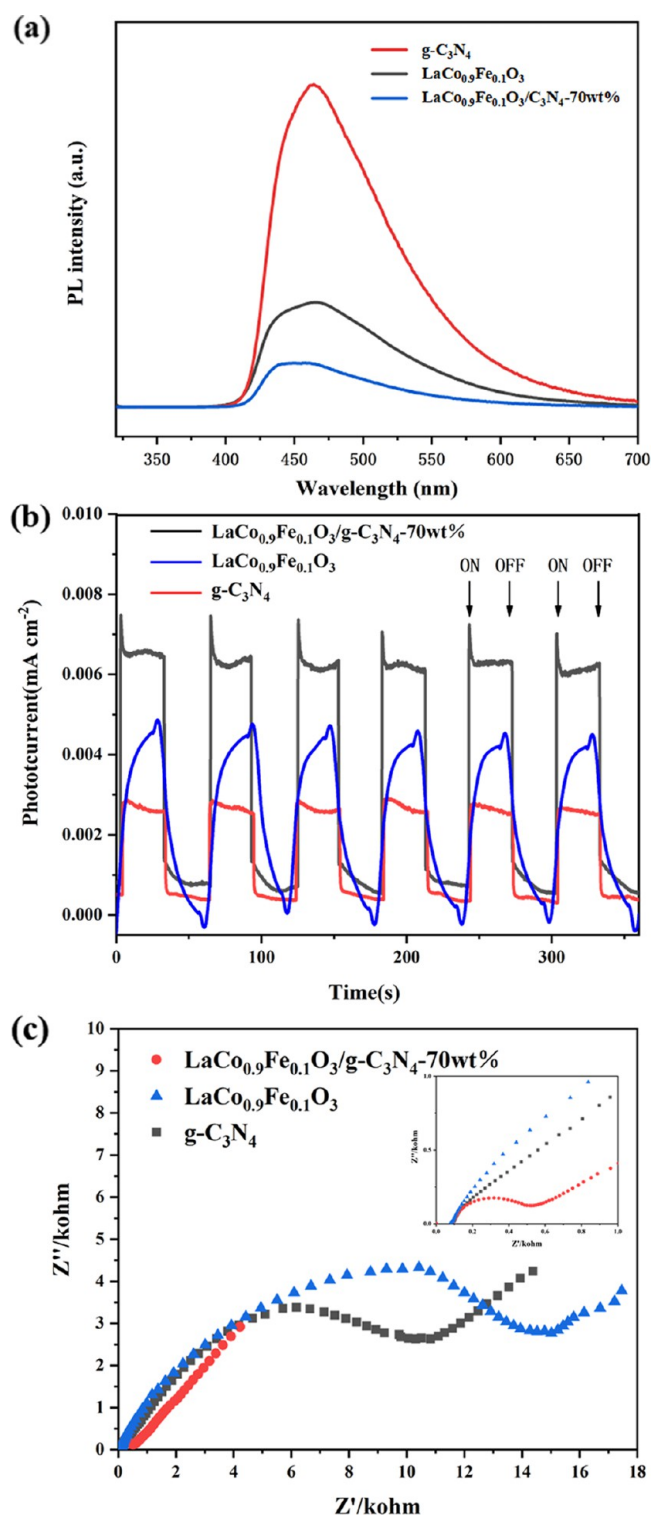
Figure 12. (a) PL spectra of $LaCo_{0.9}Fe_{0.1}O_3$, g-C_3N_4, and $LaCo_{0.9}Fe_{0.1}O_3$/g-C_3N_4-65, 70, and 75 wt % composites; (b) photocurrent spectra of $LaCo_{0.9}Fe_{0.1}O_3$, g-C_3N_4, and La-$Co_{0.9}Fe_{0.1}O_3$/g-C_3N_4-70 wt %; and (c) response of EIS.

$LaCo_{0.9}Fe_{0.1}O_3$ and g-C_3N_4 can be obtained and are approximately 5.60 and 4.63 eV, respectively. E^θ is the energy of a free electron with a hydrogen scale (~4.5 eV relative to NHE), and E_g is the band gap energy of the semiconductor.

The values of χ, ECB, and EVB are calculated and displayed in Table 3. The results show that the CB edge potential of g-

C_3N_4 (−1.42 eV) is more negative than that of $LaCo_{0.9}Fe_{0.1}O_3$ (−0.02 eV), while the VB edge potential of $LaCo_{0.9}Fe_{0.1}O_3$ (2.22 eV) is more positive than that of g-C_3N_4 (1.68 eV). The M−S curves of $LaCo_{0.9}Fe_{0.1}O_3$ and g-C_3N_4 exhibit positive slopes, indicating their n-type semiconductor nature (Figure 11e,f), which is in agreement with the reported results. Furthermore, the flat-band potentials (E_f) of g-C_3N_4 (−1.32 V vs Ag/AgCl) and $LaCo_{0.9}Fe_{0.1}O_3$ (0.08 V vs Ag/AgCl) were obtained from the M−S plots (Figure 11e,f). Considering that the voltage discrepancy between the E_{CB} and E_f of an n-type semiconductor is approximately 0.1 V, the E_{CB} of g-C_3N_4 and $LaCo_{0.9}Fe_{0.1}O_3$ is calculated to be −1.42 and −0.02 eV (vs NHE), respectively. Therefore, this is consistent with empirical formulas used for the calculation of VB and CB potentials. Distinctly, the well-matched band structures of $LaCo_{0.9}Fe_{0.1}O_3$ and g-C_3N_4 for Z-scheme charge transfer can be established after the rational construction of the $LaCo_{0.9}Fe_{0.1}O_3$/g-C_3N_4 heterojunction.

3.8. Photocurrent Response Test. The separation and transfer efficiency of photogenerated charge carriers can be evaluated by PL spectroscopy. The higher the PL signal intensity, the higher the recombination rate. The lower the PL signal intensity, the lower the recombination rate.[52] The peak height of the fluorescence spectrum is directly related to the recombination rate of the hole pair, and the stronger the intensity, the higher the recombination rate. Figure 12a shows the results of excitation of $LaCo_{0.9}Fe_{0.1}O_3$, g-C_3N_4, and $LaCo_{0.9}Fe_{0.1}O_3$/g-C_3N_4 composites with various weight ratios by light at 300 nm. We can clearly see that pure g-C_3N_4 has a strong emission peak, but under excitation at 300 nm, pure $LaCo_{0.9}Fe_{0.1}O_3$ has almost no fluorescence response signal. The fluorescence response signal of the composite of $LaCo_{0.9}Fe_{0.1}O_3$ and g-C_3N_4 was significantly lower than that of pure g-C_3N_4, indicating that the composite ratio of the composite decreased, and the fluorescence response signal of $LaCo_{0.9}Fe_{0.1}O_3$/g-C_3N_4-70 wt % was the lowest. The results show that it has the lowest carrier recombination rate and improves the activity of photocatalytic decomposition of water. Furthermore, the edge of the fluorescent band of the $LaCo_{0.9}Fe_{0.1}O_3$/g-C_3N_4 composite was blue-shifted compared with that of pure g-C_3N_4, and it was clear that there was an interaction between $LaCo_{0.9}Fe_{0.1}O_3$ and g-C_3N_4. The PL spectra show that the recombination of carriers in $LaCo_{0.9}Fe_{0.1}O_3$/g-C_3N_4 composites is greatly inhibited, which is mainly due to the photogenerated electrons in the $LaCo_{0.9}Fe_{0.1}O_3$ conduction band tending to migrate down to the valence band. g-C_3N_4 is irradiated by full-wavelength light and forms a Z-type heterostructure, which effectively inhibits the direct recombination of electron−hole pairs.

Light-induced electron transfer analysis, shown in Figure 12b, revealed a current response under light illumination with pure $LaCo_{0.9}Fe_{0.1}O_3$, g-C_3N_4, and $LaCo_{0.9}Fe_{0.1}O_3$/g-C_3N_4-70 wt %. Pure $LaCo_{0.9}Fe_{0.1}O_3$ and g-C_3N_4 revealed a small current response under light illumination; however, $LaCo_{0.9}Fe_{0.1}O_3$/g-C_3N_4-70 wt % showed a very large, rapidly rising, and stable current response, and the current response remained unchanged after multiple cycles without attenuation or time delay. Among them, the $LaCo_{0.9}Fe_{0.1}O_3$/g-C_3N_4-70 wt % composites had a photocurrent density of 0.066 mA cm^{-2}, which was higher than that of $LaCo_{0.9}Fe_{0.1}O_3$ (0.047 mA cm^{-2}) and g-C_3N_4 (0.028 mA cm^{-2}). It showed the strongest transient photocurrent response. Photocurrent is formed by the diffusion of photogenerated electrons to the back contacts,
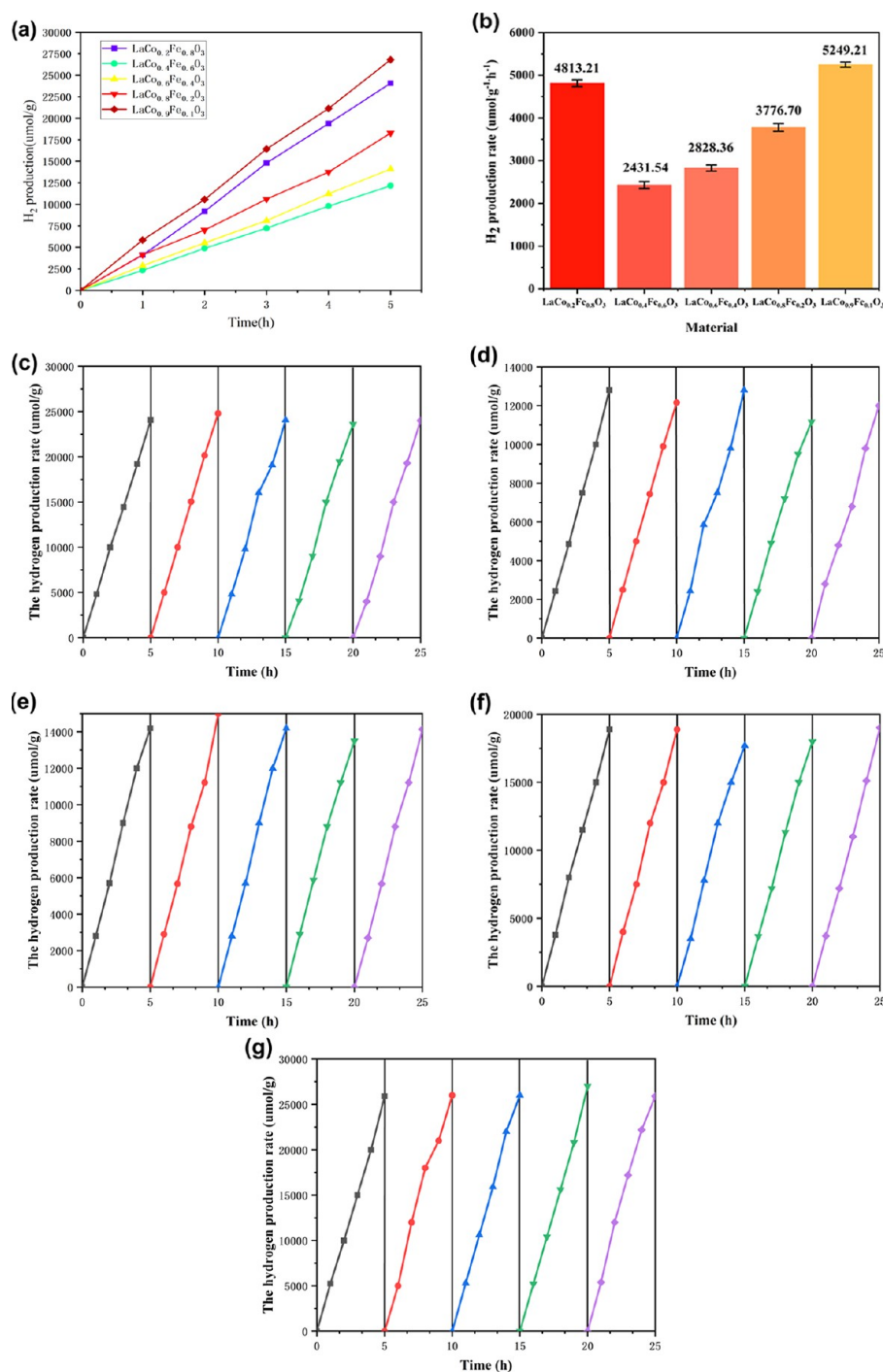
Figure 13. (a) Photocatalytic hydrogen evolution rate as a function of irradiation time of $LaCo_xFe_{1-x}O_3$ (x = 0.20, 0.40, 0.60, 0.80, and 0.90) for water splitting under full-spectrum light irradiation; (b) average hydrogen production rate of various materials per hour; and (c−g) long-term stability test of $LaCo_xFe_{1-x}O_3$ (x = 0.20, 0.40, 0.60, 0.80, and 0.90) for 20 h.

and the holes are absorbed by the hole receptors in the electrolyte.[53] Therefore, the $LaCo_{0.9}Fe_{0.1}O_3$/g-C_3N_4-70 wt % composite has a higher photogenerated electron−hole separation efficiency.

The resistance of carrier migration can be further studied by EIS. On this basis, the electronic impedance (EIS) responses of $LaCo_{0.9}Fe_{0.1}O_3$/g-C_3N_4-70 wt % and pure $LaCo_{0.9}Fe_{0.1}O_3$, g-C_3N_4 were further measured. The intersection of the semicircle with the X-axis in the pure g-C_3N_4 and pure $LaCo_{0.9}Fe_{0.1}O_3$ maps is larger than that in the composite photocatalyst, which

means that charge carrier migration will encounter greater resistance, as shown in Figure 11c. That is, the charge transfer resistance of $LaCo_{0.9}Fe_{0.1}O_3$/g-C_3N_4-70 wt % is lower than that of $LaCo_{0.9}Fe_{0.1}O_3$ and g-C_3N_4, and $LaCo_{0.9}Fe_{0.1}O_3$/g-C_3N_4-70 wt % has the lowest impedance. It was proven that the $LaCo_{0.9}Fe_{0.1}O_3$/g-C_3N_4-70 wt % carrier migration resistance was lower, and photogenerated carrier migration was more likely to occur.[54] This result proved that the $LaCo_{0.9}Fe_{0.1}O_3$/g-C_3N_4-70 wt % composite photocatalyst had a higher hydrogen
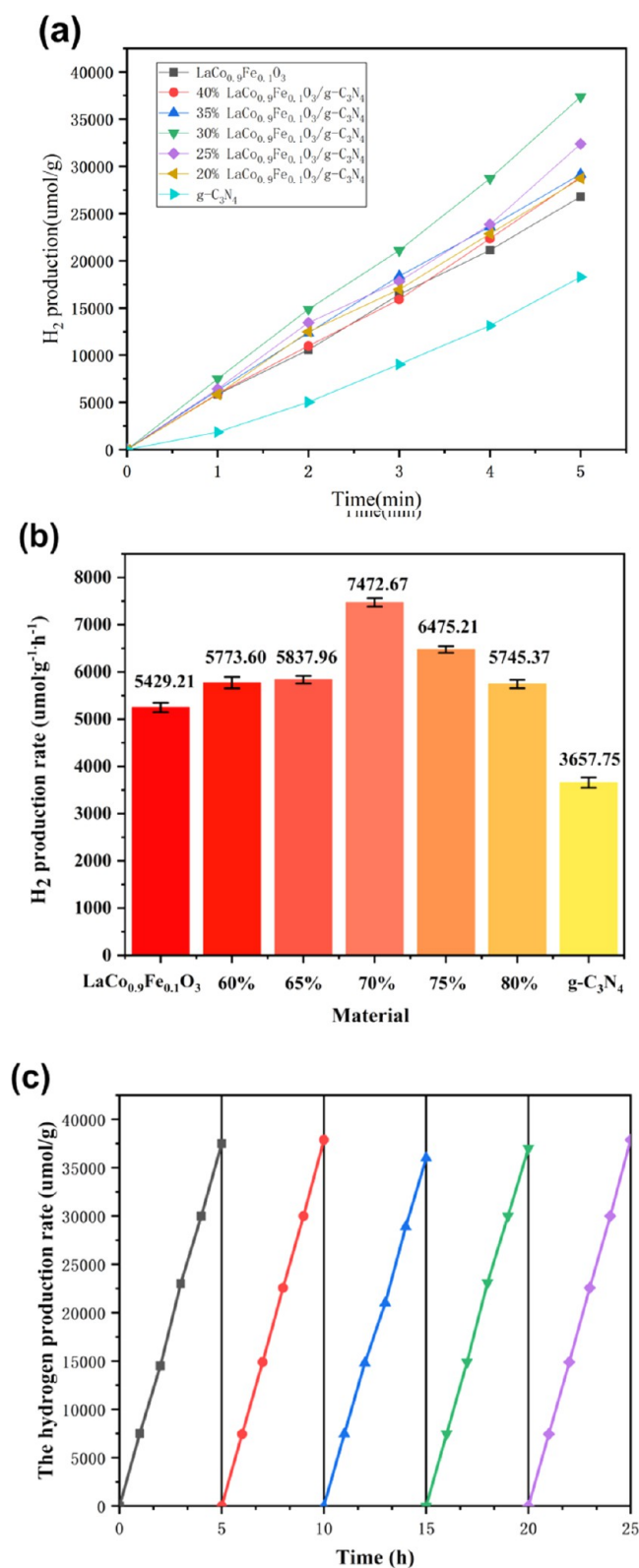
(a)

(b)

(c)

Figure 14. (a) Photocatalytic hydrogen evolution rate as a function of irradiation time of g-C$_3$N$_4$, LaCo$_{0.9}$Fe$_{0.1}$O$_3$ and 20, 25, 30, 35, and 40 wt %-LaCo$_{0.9}$Fe$_{0.1}$O$_3$/g-C$_3$N$_4$ for water splitting under full-spectrum light irradiation; (b) average hydrogen production rate of various materials per hour; and (c) long-term stability test of LaCo$_{0.9}$Fe$_{0.1}$O$_3$/g-C$_3$N$_4$-70 wt % for 20 h.

production efficiency and could inhibit the recombination of photogenerated electron−hole pairs more effectively.
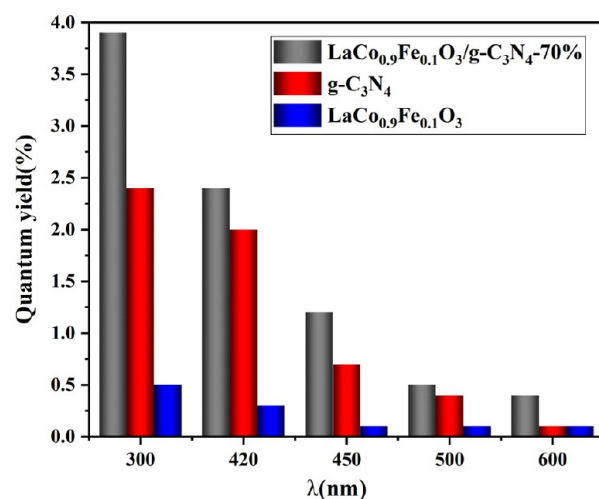

Figure 15. AQY of LaCo$_{0.9}$Fe$_{0.1}$O$_3$/g-C$_3$N$_4$-70 wt %, g-C$_3$N$_4$, and LaCo$_{0.9}$Fe$_{0.1}$O$_3$ composites under different wavelengths of 300, 420, 450, 500, and 600 nm.

3.9. Photocatalytic Performance Test. First of all, we conducted a blank control test, carrying it out without full-spectrum light and photocatalyst to evaluate the effect of light and photocatalyst on the experiment. Under this premise, the photolysis efficiency is not worth considering, which shows that TES water containing 20% methanol is stable under visible light irradiation. Then, anhydrous control experiments were conducted to eliminate the possibility of methanol reforming in the full-spectrum range. 20 mL of methanol and 10 mg of the LaCo$_{0.9}$Fe$_{0.1}$O$_3$ catalyst were added to the photocatalytic experiment. The results showed hydrogen generation is not worth considering, which could be ignored. This shows that methanol just consumes holes to promote photocatalytic hydrogen production. Then, the photocatalytic properties of LaCo$_x$Fe$_{1-x}$O$_3$ (x = 0.20, 0.40, 0.60, 0.80, and 0.90) nanoparticles were measured in aqueous solution with 20% (volume) methanol as the sacrificial reagent under full-spectrum (250−1200 nm) irradiation of a 300 W xenon lamp. H$_2$ emissions were detected using gas chromatography, as shown in Figure 13a,b. We performed three parallel tests on all samples, as shown in Figure 13c−g, and calculated the average hydrogen production rate, which could eliminate unexpected factors and obtain more convincing data. Obviously, we can see that the materials have various hydrogen production rates with various Fe doping ratios. The hydrogen release rates of LaCo$_x$Fe$_{1-x}$O$_3$ (x = 0.20, 0.40, 0.60, 0.80, and 0.90) are 4813.21, 2431.54, 2828.36, 3776.70, and 5249.21 μmol h^{-1} g^{-1}, respectively. LaCo$_{0.9}$Fe$_{0.1}$O$_3$ has the highest photocatalytic activity, with an average hydrogen production of 5249.21 μmol h^{-1} g^{-1}, which is 17.60 times higher than that of LaCoO$_3$ without Fe doping.[24] As shown in Figure 13c, the photocatalytic efficiency did not show a significant loss even after five consecutive cycles, which suggests that under the irradiation of a xenon lamp, the catalyst is highly stable in the process of photocatalytic hydrolysis. The photocatalytic properties of LaCo$_{0.9}$Fe$_{0.1}$O$_3$/g-C$_3$N$_4$ nanoparticles with various mass ratios were tested. H$_2$ emissions were detected using gas chromatography, as shown in Figure 14a,b. We performed three parallel tests on all samples and calculated the average hydrogen production rate, which eliminates the element of surprise and yields more convincing data. By calculating the errors, it was confirmed that the repeatability
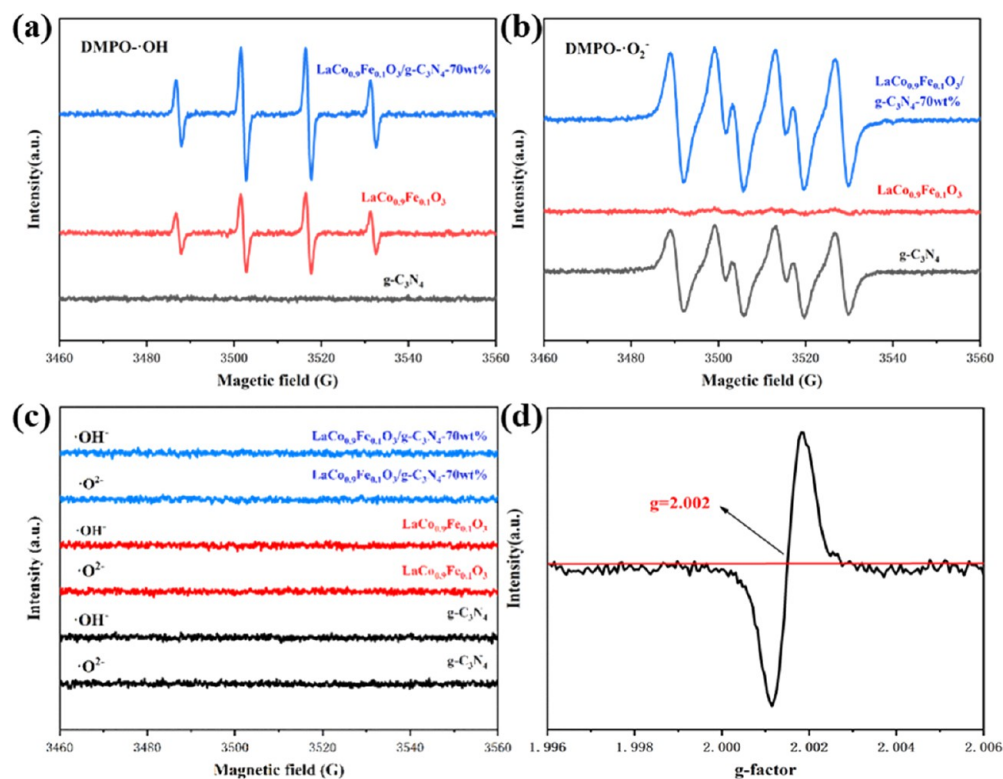
Figure 16. Pure g-C_3N_4, $LaCo_{0.9}Fe_{0.1}O_3$, and $LaCo_{0.9}Fe_{0.1}O_3$/g-C_3N_4-70 wt % complex were irradiated in (a) aqueous dispersion (for DMPO-$\cdot O_2^-$) and (b) aqueous dispersion (for DMPO-$\cdot OH^-$) under full spectrum with a xenon lamp; (c) EPR spectra of g-C_3N_4, $LaCo_{0.9}Fe_{0.1}O_3$, and $LaCo_{0.9}Fe_{0.1}O_3$/g-C_3N_4-70 wt % in the dark; (d) g value of the $LaCo_{0.9}Fe_{0.1}O_3$/g-C_3N_4-70 wt % complex.
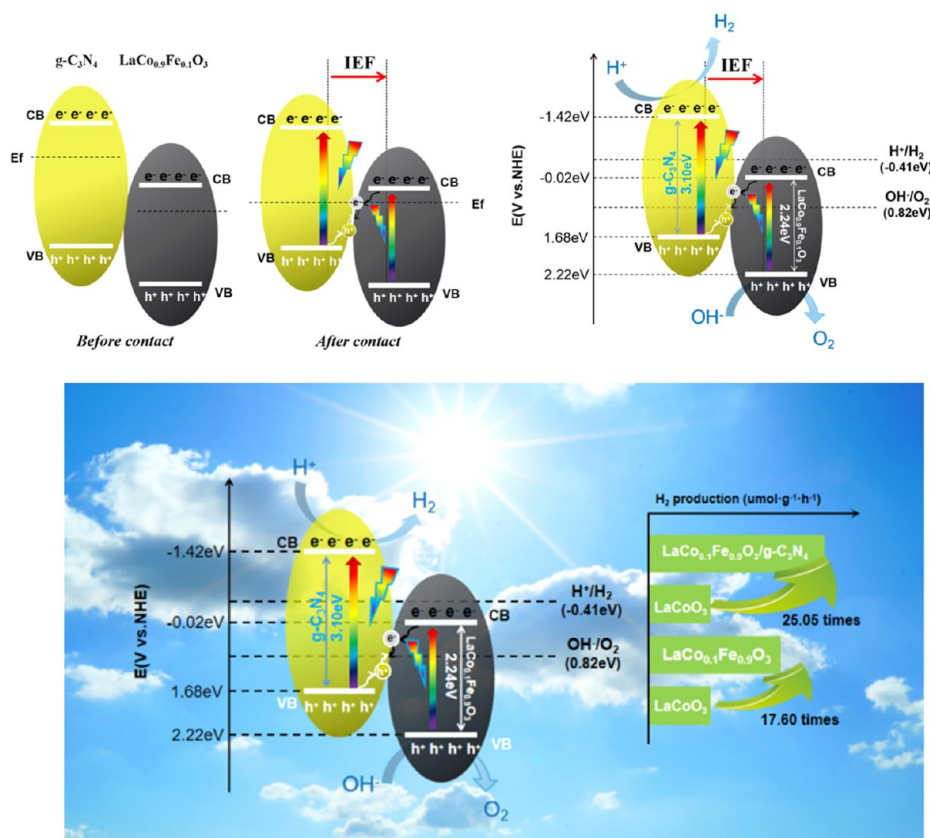
Figure 17. Z-scheme heterojunction of $LaCo_{0.9}Fe_{0.1}O_3$/g-C_3N_4 before contact interaction; after contact interaction, and after contact interaction under irradiation, photogenerated carrier migration and separation, and photocatalytic hydrogen evolution.

and reproducibility of the data were maintained at a level of 0.02% or less. Clearly, the prepared g-C_3N_4, $LaCo_{0.9}Fe_{0.1}O_3$, and $LaCo_{0.9}Fe_{0.1}O_3$/g-C_3N_4-60, 65, 70, 75, and 80 wt % composites have various levels of hydrogen production by photolysis. The hydrogen rates of $LaCo_{0.9}Fe_{0.1}O_3$ and g-C_3N_4 were 5249.21 and 3657.75 μmol h^{-1} g^{-1}. $LaCo_{0.9}Fe_{0.1}O_3$/g-C_3N_4-70 wt % composites had the highest photocatalytic activity, with an average hourly hydrogen production of 7472.67 μmol h^{-1} g^{-1}, which was 1.5 and 2.0 times higher than that of $LaCo_{0.9}Fe_{0.1}O_3$ and g-C_3N_4, respectively, and 7.14 times that of $LaCo_{0.9}Fe_{0.1}O_3$/g-C_3N_4 without Fe doping.[24] As shown in Figure 14c, there was no apparent loss of photocatalytic efficiency even after five consecutive cycles, which suggests that under full-spectrum irradiation of the Xenon lamp, the heterojunction photocatalyst is highly stable in the process of photocatalytic hydrolysis. The AQY of $LaCo_{0.9}Fe_{0.1}O_3$/g-C_3N_4-70 wt % is 3.9%, 2.4, 1.2, 0.5, and 0.4% at 300, 420, 450, 500, and 600 nm, respectively, as shown in Figure 15.

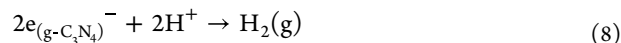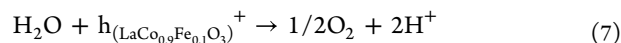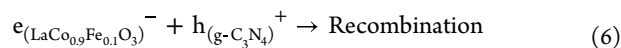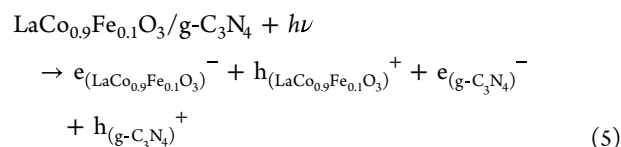**3.10. Electron Paramagnetic Resonance Spectroscopy.** To understand the mechanism of the reaction, we carried out electron paramagnetic resonance (EPR) spectroscopy. As shown in Figure 16a, after 10 min of exposure to xenon lamp full-spectrum light, $^{\bullet}$OH free radical signals of $LaCo_{0.9}Fe_{0.1}O_3$ and $LaCo_{0.9}Fe_{0.1}O_3$/g-C_3N_4-70 wt % can be observed; no $^{\bullet}$OH free radical signal was observed for pure g-C_3N_4. The absence of a DMPO-$^{\bullet}$OH signal in g-C_3N_4 is because $^{\bullet}$OH cannot be generated from a hole in the VB in g-C_3N_4 (EVB = 1.68 eV, $E^{\theta}_{OH-/^{\bullet}OH}$ = 1.99 eV vs NHE). Observations of the DMPO-$^{\bullet}$OH signal of the $LaCo_{0.9}Fe_{0.1}O_3$/g-C_3N_4-70 wt % complex indicate that the photogenerated hole remains in the VB of $LaCo_{0.9}Fe_{0.1}O_3$ and does not transfer to the VB of g-C_3N_4. In Figure 16b, DMPO-$^{\bullet}O^{2-}$ signals of g-C_3N_4 and $LaCo_{0.9}Fe_{0.1}O_3$/g-C_3N_4-70 wt % composite samples could be observed after 10 min of exposure to xenon lamp full-spectrum light, and $^{\bullet}O_2^{-}$ signals of $LaCo_{0.9}Fe_{0.1}O_3$ could not be observed. As Figure 16c shows, $LaCo_{0.9}Fe_{0.1}O_3$, g-C_3N_4 and $LaCo_{0.9}Fe_{0.1}O_3$/g-C_3N_4-70 wt % possess no ESR signals in the dark, which proves that both $^{\bullet}O^{2-}$ and $^{\bullet}$OH are excited by visible light. The results show that the photogenerated electrons in the g-C_3N_4 and $LaCo_{0.9}Fe_{0.1}O_3$/g-C_3N_4-70 wt % composite samples have sufficient reduction ability to reduce O_2 to form superoxide radical anions (O_2^{-}) ($E^{\theta}_{O_2/^{\bullet}O_2^{-}}$ = −0.33 eV vs NHE). By calculation, we derive a g value of 2.002 for the $LaCo_{0.9}Fe_{0.1}O_3$/g-C_3N_4-70 wt % complex, as evidenced by the presence of an oxygen vacancy in the complex in Figure 16d.[55,56] On the basis of the above characterizations and analyses, the Z-scheme charge transfer mechanism for $LaCo_{0.9}Fe_{0.1}O_3$/g-C_3N_4 in the photocatalytic hydrogen evolution (Figure 17). The EPR can prove that photogenerated electrons and holes exist in the CB and VB of $LaCo_{0.9}Fe_{0.1}O_3$ and g-C_3N_4, respectively, and at the same time, charge transfer does not match the conventional type II heterojunction mechanism. It can be inferred that the charge transfer path of this reaction is a Z-type mechanism. Both $LaCo_{0.9}Fe_{0.1}O_3$ and g-C_3N_4 have band gap widths, and when the photon energy is equal to or greater than the band gap width, the photogenerated electrons transition from the VB of g-C_3N_4 and $LaCo_{0.9}Fe_{0.1}O_3$ to the CB and create holes in the valence band [eq 5]. Then, electrons on $LaCo_{0.9}Fe_{0.1}O_3$ rapidly recombine with holes on g-C_3N_4 via a heterostructure [eq 6]. Water and holes combine to produce hydrogen ions and oxygen [eq 7], and hydrogen ions further combine with electrons in the g-

C_3N_4 conduction band to produce hydrogen [eq 8]. The specific process of photocatalysis is as follows

$$LaCo_{0.9}Fe_{0.1}O_3/g\text{-}C_3N_4 + h\nu$$
$$\rightarrow e_{(LaCo_{0.9}Fe_{0.1}O_3)}^{-} + h_{(LaCo_{0.9}Fe_{0.1}O_3)}^{+} + e_{(g\text{-}C_3N_4)}^{-}$$
$$+ h_{(g\text{-}C_3N_4)}^{+} \tag{5}$$

$$e_{(LaCo_{0.9}Fe_{0.1}O_3)}^{-} + h_{(g\text{-}C_3N_4)}^{+} \rightarrow \text{Recombination} \tag{6}$$

$$H_2O + h_{(LaCo_{0.9}Fe_{0.1}O_3)}^{+} \rightarrow 1/2O_2 + 2H^{+} \tag{7}$$

$$2e_{(g\text{-}C_3N_4)}^{-} + 2H^{+} \rightarrow H_2(g) \tag{8}$$

4. CONCLUSIONS

Fe-doped $LaCo_xFe_{1-x}O_3$ nanocomposites were successfully prepared by the sol−gel method. A $LaCo_{0.9}Fe_{0.1}O_3$/g-C_3N_4 nanoheterojunction photocatalyst was successfully prepared to improve the semiconductor performance, and the photocatalytic activity was significantly increased. The existence of doped "Fe" was confirmed by XRD and EDS spectra. The chemical oxidation states of various elements in the photocatalysts were determined by XPS. A series of characterization results showed that $LaCo_{0.9}Fe_{0.1}O_3$ was in the form of 60−90 nm nanospheres, and g-C_3N_4 had a layered structure with a good appearance. The results showed that $LaCo_{0.9}Fe_{0.1}O_3$ nanoparticles were successfully compounded with g-C_3N_4 nanosheets. Under photocatalysis conditions, the highest photocatalytic activity of $LaCo_{0.9}Fe_{0.1}O_3$/g-C_3N_4-70 wt % was 7472.67 μmol h^{-1} g^{-1}, which was 7.14 times higher than that of $LaCo_3$/g-C_3N_4 without Fe doping. The photocatalytic activity of $LaCo_{0.9}Fe_{0.1}O_3$/g-C_3N_4 was significantly higher than that of the other catalysts.[24,57,58] This study not only designed a low-cost and high-efficiency $LaCo_{0.9}Fe_{0.1}O_3$/g-C_3N_4 photocatalytic system for water cracking or other photocatalytic applications but also provided a new idea for the construction of new materials for photocatalysis.

■ ASSOCIATED CONTENT

Ⓢ Supporting Information

The Supporting Information is available free of charge at https://pubs.acs.org/doi/10.1021/acsomega.3c01393.

Fabrication procedure of the $LaCo_{0.9}Fe_{0.1}O_3$/g-C_3N_4 Z-scheme heterojunctions; comparison and summary of other photocatalyst systems for photocatalytic H_2 evolution; and all data generated or analyzed during this study (PDF)

■ AUTHOR INFORMATION

Corresponding Author

Fubin Jiang − *College of Chemistry, Beijing Normal University, Beijing 100875, China; Department of Chemistry, Faculty of Arts and Sciences, Beijing Normal University, Zhuhai 519087, China;* ⓘ orcid.org/0000-0003-2120-2827; Phone: +86 01058802850; Email: jfb@bnu.edu.cn

Authors

Kexin Zhang − *College of Chemistry, Beijing Normal University, Beijing 100875, China;* ⓘ orcid.org/0009-0002-5523-2477

Rui Wang − *College of Chemistry, Beijing Normal University, Beijing 100875, China; Institute of Chemical Engineering and Technology, Xi'an Jiaotong University, Xi'an 710049, China*

Author Contributions

K.Z. was the main author of the work, who performed syntheses and electron microscopy and coordinated all characterization and catalytic studies. R.W. was responsible for part of the synthesis work, and F.J. assisted with manuscript writing. All authors read and approved the final manuscript.

Notes

The authors declare no competing financial interest.

■ REFERENCES

(1) Chakraborty, S.; Dash, S. K.; Elavarasan, R. M.; Kaur, A.; Elangovan, D.; Meraj, S. T.; Kasinathan, P.; Said, Z. Hydrogen energy as future of sustainable mobility. *Front. Energy Res.* **2022**, *10*, 10.

(2) Farias, C. B. B.; Barreiros, R. C. S.; Da Silva, M. F.; Casazza, A. A.; Converti, A.; Sarubbo, L. A. Use of hydrogen as fuel: a trend of the 21st century. *Energies* **2022**, *15*, 311.

(3) Ishaq, H.; Dincer, I.; Crawford, C. A review on hydrogen production and utilization: challenges and opportunities. *Int. J. Hydrogen Energy* **2022**, *47*, 26238−26264.

(4) Saiful Islam, M. Ionic transport in ABO_3 perovskite oxides: a computer modelling tour. *J. Mater. Chem.* **2000**, *10*, 1027−1038.

(5) Zhang, L.; Hu, J.; Song, P.; Qin, H.; Jiang, M. Electrical properties and ethanol-sensing characteristics of perovskite $La_{1-x}Pb_xFeO_3$. *Sens. Actuators, B* **2006**, *114*, 836−840.

(6) Chávez-Guerrero, L.; Medina-Lott, B.; Cienfuegos, R. F.; Garza-Navarro, M. A.; Vannier, R. N.; Ringuedé, A.; Hinojosa, M.; Cassir, M. Synthesis and characterization of $LaNi_xCo_{1-x}O_3$: role of microstructure on magnetic properties. *J. Rare Earths* **2015**, *33*, 277−281.

(7) C C B Oliveira, L.; Venâncio, R.; V F de Azevedo, P.; Anchieta, C. G.; C M Nepel, T.; Rodella, C. B.; Zanin, H.; Doubek, G.; Rodella, C. B.; Zanin, H.; Doubek, G. Reviewing perovskite oxide sites influence on electrocatalytic reactions for high energy density devices. *J. Energy Chem.* **2023**, *81*, 1−19.

(8) Wang, F.; Wu, Y.; Zhao, Y.; Zhou, M.; Tang, S.; Ji, G. The effect of sr doping on the electronic structure and electromagnetic properties of $LaCo_{0.9}Fe_{0.1}O_3$ perovskites. *Inorg. Chem. Front.* **2022**, *9*, 5745−5756.

(9) Li, H.; Li, J.; Ai, Z.; Jia, F.; Zhang, L. Durch sauerstoff-leerstellen vermittelte photokatalyse mit biocl: reaktivität, selektivität und ausblick. *Angew. Chem.* **2018**, *130*, 128−145.

(10) Li, X.; Li, K.; Ding, D.; Yan, J.; Wang, C.; Carabineiro, S. A. C.; Liu, Y.; Lv, K. Effect of oxygen vacancies on the photocatalytic activity of flower-like BiOBr microspheres towards no oxidation and Co_2 reduction. *Sep. Purif. Technol.* **2023**, *309*, 123054.

(11) Lee, I.; Jung, B.; Park, J.; Lee, C.; Hwang, J.; Park, C. O. Mixed potential NH_3 sensor with $LaCoO_3$ reference electrode. *Sens. Actuators, B* **2013**, *176*, 966−970.

(12) Zhang, K.; Xie, A.; Sun, M.; Jiang, W.; Wu, F.; Dong, W. Electromagnetic dissipation on the surface of metal organic framework (MOF)/reduced graphene oxide (RGO) hybrids. *Mater. Chem. Phys.* **2017**, *199*, 340−347.

(13) Ding, J.; Li, H.; Guo, X. Co sensing mechanism of $LaCoO_3$. *Solid State Ionics* **2015**, *272*, 155−159.

(14) Augustinsky, P.; Krapek, V.; Kunes, J. Doping induced spin state transition in $LaCoO_3$: dynamical mean-field study. *Phys. Rev. Lett.* **2013**, *110*, 267204.

(15) Madi, M.; Tahir, M. Highly stable $LaCoO_3$ perovskite supported g-C_3N_4 nanotextures with proficient charges migration for visible light CO_2 photoreduction to co and CH_4. *Mater. Sci. Semicond. Process.* **2022**, *142*, 106517.

(16) Xie, W.; Xu, G.; Zhang, Y.; Yu, Y.; He, H. Mesoporous $LaCoO_3$ perovskite oxide with high catalytic performance for no storage and reduction. *J. Hazard. Mater.* **2022**, *431*, 128528.

(17) Tang, M.; Ao, Y.; Wang, C.; Wang, P. Facile synthesis of dual Z-scheme g-C3N4/Ag3PO4/AgI composite photocatalysts with enhanced performance for the degradation of a typical neonicotinoid pesticide. *Appl. Catal., B* **2020**, *268*, 118395.

(18) Li, Z.; Xie, Y.; Huang, Z.; Su, Y.; Sun, C.; Fu, J.; Wei, H.; Wu, F.; Ou, G. Amorphization of lacoo3 perovskite nanostructures for efficient oxygen evolution. *ACS Appl. Nano Mater.* **2022**, *5*, 14209−14215.

(19) Tang, C.; Zhang, R.; Lu, W.; He, L.; Jiang, X.; Asiri, A. M.; Sun, X. Fe-doped cop nanoarray: a monolithic multifunctional catalyst for highly efficient hydrogen generation. *Adv. Mater.* **2017**, *29*, 1602441.

(20) Wan, C.; Leonard, B. M. Iron-doped molybdenum carbide catalyst with high activity and stability for the hydrogen evolution reaction. *Chem. Mat.* **2015**, *27*, 4281−4288.

(21) Dholam, R.; Patel, N.; Adami, M.; Miotello, A. Hydrogen production by photocatalytic water-splitting using Cr- or Fe-doped TiO_2 composite thin films photocatalyst. *Int. J. Hydrogen Energy* **2009**, *34*, 5337−5346.

(22) Hu, S.; Jia, L.; Chi, B.; Pu, J.; Jian, L. Visible light driven (Fe, Cr)-Codoped $La_2Ti_2O_7$ photocatalyst for efficient photocatalytic hydrogen production. *J. Power Sources* **2014**, *266*, 304−312.

(23) Siritanaratkul, B.; Maeda, K.; Hisatomi, T.; Domen, K. Synthesis and Photocatalytic Activity of Perovskite Niobium Oxynitrides with Wide Visible-Light Absorption Bands. *ChemSusChem* **2011**, *4*, 74−78.

(24) Wang, R.; Ye, C.; Wang, H.; Jiang, F. Z-scheme $LaCoO_3$/g-C_3N_4 for efficient full-spectrum light-simulated solar photocatalytic hydrogen generation. *ACS Omega* **2020**, *5*, 30373−30382.

(25) Wang, R.; Zhang, K.; Zhong, X.; Jiang, F. Z-scheme LaCoO(3)/C(3)N(5) for efficient full-spectrum light-simulated solar photocatalytic hydrogen generation. *RSC Adv.* **2022**, *12*, 24026−24036.

(26) Zhang, Z.; Wang, W.; Gao, E.; Shang, M.; Xu, J. Enhanced photocatalytic activity of Bi_2WO_6 with oxygen vacancies by zirconium doping. *J. Hazard. Mater.* **2011**, *196*, 255−262.

(27) Wan, G.; Yin, L.; Chen, X.; Xu, X.; Huang, J.; Zhen, C.; Zhu, H.; Huang, B.; Hu, W.; Ren, Z.; et al. Photocatalytic overall water splitting over $PbTiO_3$ modulated by oxygen vacancy and ferroelectric polarization. *J. Am. Chem. Soc.* **2022**, *144*, 20342−20350.

(28) Yang, Y.; Zhao, S.; Bi, F.; Chen, J.; Li, Y.; Cui, L.; Xu, J.; Zhang, X. Oxygen-vacancy-induced O_2 activation and electron-hole migration enhance photothermal catalytic toluene oxidation. *Cell Rep. Phys. Sci.* **2022**, *3*, 101011.

(29) Li, L.; Ma, Y.; Chen, G.; Wang, J.; Wang, C. Oxygen-vacancy-enhanced piezo-photocatalytic performance of $AgNbO_3$. *Scr. Mater.* **2022**, *206*, 114234.

(30) Bak, J.; Bin Bae, H.; Chung, S. Atomic-scale perturbation of oxygen octahedra via surface ion exchange in perovskite nickelates boosts water oxidation. *Nat. Commun.* **2019**, *10*, 2713.

(31) Yang, S.; Li, H.; Li, H.; Li, H.; Qi, W.; Zhang, Q.; Zhu, J.; Zhao, P.; Chen, L. Rational design of 3d carbon nitrides assemblies with tunable nano-building blocks for efficient visible-light photocatalytic CO_2 conversion. *Appl. Catal., B* **2022**, *316*, 121612.

(32) Maridevaru, M. C.; Anandan, S.; Aljafari, B.; Wu, J. J. $LaCo_xFe_{1-x}O_3$ ($0 \leq x \leq 1$) spherical nanostructures prepared via ultrasonic approach as photocatalysts. *Ultrason. Sonochem.* **2021**, *80*, 105824.

(33) Duan, Y.; Sun, S.; Xi, S.; Ren, X.; Zhou, Y.; Zhang, G.; Yang, H.; Du, Y.; Xu, Z. J. Tailoring the co 3d-o 2p covalency in LaCoO3 by Fe substitution to promote oxygen evolution reaction. *Chem. Mat.* **2017**, *29*, 10534−10541.

(34) Bouich, A.; Marí-Guaita, J.; Soucase, B. M.; Palacios, P. Bright future by enhancing the stability of methylammonium lead triiodide

perovskites thin films through Rb, Cs and Li as dopants. *Mater. Res. Bull.* **2023**, *163*, 112213.

(35) Xiao, C.; Lu, X.; Zhao, C. Unusual synergistic effects upon incorporation of Fe and/or Ni into mesoporous Co_3O_4 for enhanced oxygen evolution. *Chem. Commun.* **2014**, *50*, 10122−10125.

(36) Dong, G.; Zhang, L. Porous structure dependent photoreactivity of graphitic carbon nitride under visible light. *J. Mater. Chem.* **2012**, *22*, 1160−1166.

(37) Wang, F.; Gu, W.; Chen, J.; Wu, Y.; Zhou, M.; Tang, S.; Cao, X.; Zhang, P.; Ji, G. The point defect and electronic structure of k doped $LaCo_{0.9}Fe_{0.1}O_3$ perovskite with enhanced microwave absorbing ability. *Nano Res.* **2022**, *15*, 3720−3728.

(38) Qi, L.; Tang, X.; Wang, Z.; Peng, X. Pore characterization of different types of coal from coal and gas outburst disaster sites using low temperature nitrogen adsorption approach. *Int. J. Min. Sci. Technol.* **2017**, *27*, 371−377.

(39) Lv, Q.; Cao, C.; Li, C.; Zhang, J.; Zhu, H.; Kong, X.; Duan, X. Formation of crystalline carbon nitride powder by a mild solvothermal method. *J. Mater. Chem.* **2003**, *13*, 1241.

(40) Zhang, B.; Liu, J.; Yue, S.; Teng, Y.; Wang, Z.; Li, X.; Qu, S.; Wang, Z. Hot electron injection: an efficacious approach to charge $LaCoO_3$ for improving the water splitting efficiency. *Appl. Catal., B* **2017**, *219*, 432−438.

(41) Pang, X.; Guo, Y.; Zhang, Y.; Xu, B.; Qi, F. Lacoo3 perovskite oxide activation of peroxymonosulfate for aqueous 2-phenyl-5-sulfobenzimidazole degradation: effect of synthetic method and the reaction mechanism. *Chem. Eng. J.* **2016**, *304*, 897−907.

(42) Li, Y.; Liu, Y.; Wang, J.; Guo, Y.; Chu, K. Plasma-engineered nio nanosheets with enriched oxygen vacancies for enhanced electrocatalytic nitrogen fixation. *Inorg. Chem. Front.* **2020**, *7*, 455−463.

(43) Dacquin, J. P.; Lancelot, C.; Dujardin, C.; Da Costa, P.; Djega-Mariadassou, G.; Beaunier, P.; Kaliaguine, S.; Vaudreuil, S.; Royer, S.; Granger, P. Influence of preparation methods of $LaCoO_3$ on the catalytic performances in the decomposition of N_2O. *Appl. Catal., B* **2009**, *91*, 596−604.

(44) Dogu, D.; Meyer, K. E.; Fuller, A.; Gunduz, S.; Deka, D. J.; Kramer, N.; Co, A. C.; Ozkan, U. S. Effect of lanthanum and chlorine doping on strontium titanates for the electrocatalytically-assisted oxidative dehydrogenation of ethane. *Appl. Catal., B* **2018**, *227*, 90−101.

(45) Fang, Y.; Lang, J.; Wang, J.; Han, Q.; Zhang, Z.; Zhang, Q.; Yang, J.; Xing, S. G. Rare-earth doping engineering in nanostructured ZnO a new type of eco-friendly photocatalyst with enhanced photocatalytic characteristics. *Appl. Phys. A: Mater. Sci. Process.* **2018**, *124*, 605.

(46) Wang, K.; Niu, H.; Chen, J.; Song, J.; Mao, C.; Zhang, S.; Gao, Y. Immobilizing $LaFeO_3$ nanoparticles on carbon spheres for enhanced heterogeneous photo-fenton like performance. *Appl. Surf. Sci.* **2017**, *404*, 138−145.

(47) Lin, L.; Zhu, Q.; Xu, A. Noble-metal-free Fe-N/C catalyst for highly efficient oxygen reduction reaction under both alkaline and acidic conditions. *J. Am. Chem. Soc.* **2014**, *136*, 11027−11033.

(48) Orlovskaya, N.; Steinmetz, D.; Yarmolenko, S.; Pai, D.; Sankar, J.; Goodenough, J. Detection of temperature- and stress-induced modifications of $LaCoO_3$ by micro-raman spectroscopy. *Phys. Rev. B: Condens. Matter Mater. Phys.* **2005**, *72*, 014122−14122.

(49) Ge, Z.; Li, X.; Zhang, W.; Sun, Q.; Chai, C.; Luo, Y. Preparation and characterization of ultrafine Fe-O compound/ammonium perchlorate nanocomposites via in-suit growth method. *J. Solid State Chem.* **2018**, *258*, 138−145.

(50) Xia, P.; Liu, M.; Cheng, B.; Yu, J.; Zhang, L. Dopamine modified g-C_3N_4 and its enhanced visible-light photocatalytic H_2-production activity. *ACS Sustain. Chem. Eng.* **2018**, *6*, 8945−8953.

(51) Shang, Y.; Chen, X.; Liu, W.; Tan, P.; Chen, H.; Wu, L.; Ma, C.; Xiong, X.; Pan, J. Photocorrosion inhibition and high-efficiency photoactivity of porous g-C_3N_4/Ag_2CrO_4 composites by simple microemulsion-assisted Co-precipitation method. *Appl. Catal., B* **2017**, *204*, 78−88.

(52) Zhu, X.; Zhang, F.; Wang, M.; Ding, J.; Sun, S.; Bao, J.; Gao, C. Facile synthesis, structure and visible light photocatalytic activity of recyclable $ZnFe_2O_4$/TiO_2. *Appl. Surf. Sci.* **2014**, *319*, 83−89.

(53) Kazyrevich, M. E.; Malashchonak, M. V.; Mazanik, A. V.; Streltsov, E. A.; Kulak, A. I.; Bhattacharya, C. Photocurrent switching effect on platelet-like bioi electrodes: influence of redox system, light wavelength and thermal treatment. *Electrochim. Acta* **2016**, *190*, 612−619.

(54) Huang, J.; Xu, Z.; Zhao, S.; Li, S.; Feng, X.; Wang, P.; Zhang, Z. Study on carrier mobility measurement using electroluminescence in frequency domain and electrochemical impedance spectroscopy. *Measurement* **2010**, *43*, 295−298.

(55) Zhang, N.; Li, X.; Ye, H.; Chen, S.; Ju, H.; Liu, D.; Lin, Y.; Ye, W.; Wang, C.; Xu, Q.; et al. Oxide defect engineering enables to couple solar energy into oxygen activation. *J. Am. Chem. Soc.* **2016**, *138*, 8928−8935.

(56) Yang, J.; Hu, S.; Fang, Y.; Hoang, S.; Li, L.; Yang, W.; Liang, Z.; Wu, J.; Hu, J.; Xiao, W.; et al. Oxygen vacancy promoted O_2 activation over perovskite oxide for low-temperature Co oxidation. *ACS Catal.* **2019**, *9*, 9751−9763.

(57) Kong, L.; Dong, Y.; Jiang, P.; Wang, G.; Zhang, H.; Zhao, N. Light-assisted rapid preparation of a ni/g-c3n4 magnetic composite for robust photocatalytic H_2-evolution from water. *J. Mater. Chem. A* **2016**, *4*, 9998−10007.

(58) Han, X.; Xu, D.; An, L.; Hou, C.; Li, Y.; Zhang, Q.; Wang, H. Ni-Mo nanoparticles as co-catalyst for drastically enhanced photocatalytic hydrogen production activity over g-C_3N_4. *Appl. Catal., B* **2019**, *243*, 136−144.